POMINO-GEMS: A Research Product for Tropospheric NO_2 Columns from Geostationary Environment Monitoring Spectrometer

Yuhang Zhang[1], Jintai Lin[1], Jhoon Kim[2], Hanlim Lee[3], Junsung Park[3], Hyunkee Hong[4], Michel Van Roozendael[5], Francois Hendrick[5], Ting Wang[6,7], Pucai Wang[6,7], Qin He[8], Kai Qin[8], Yongjoo Choi[9], Yugo Kanaya[10], Jin Xu[11], Pinhua Xie[7,11], Xin Tian[12], Sanbao Zhang[13], Shanshan Wang[13], Siyang Cheng[14], Xinghong Cheng[14], Jianzhong Ma[14], Thomas Wagner[15], Robert Spurr[16], Lulu Chen[17], Hao Kong[1], Mengyao Liu[18]

[1]Laboratory for Climate and Ocean-Atmosphere Studies, Department of Atmospheric and Oceanic Sciences, School of Physics, Peking University, Beijing, 100871, China
[2]Department of Atmospheric Sciences, Yonsei University, Seoul, South Korea
[3]Pukyong National University, Busan, South Korea
[4]National Institute of Environmental Research, Incheon, South Korea
[5]Belgian Institute for Space Aeronomy (BIRA-IASB), Brussels, Belgium
[6]CNRC & LAGEO, Institute of Atmospheric Physics, Chinese Academy of Sciences, Beijing, 100029, China
[7]University of Chinese Academy of Sciences, Beijing, 100049, China
[8]School of Environment and Geoinformatics, China University of Mining and Technology, Xuzhou, Jiangsu, 221116, China
[9]Department of Environmental Science, Hankuk University of Foreign Studies, Yongin, South Korea
[10]Research Institute for Global Change, Japan Agency for Marine-Earth Science and Technology (JAMSTEC), Yokohama, 2360001, Japan
[11]Key Laboratory of Environmental Optics and Technology, Anhui Institute of Optics and Fine Mechanics, Chinese Academy of Science, Hefei, 230031, China
[12]Information Materials and Intelligent Sensing Laboratory of Anhui Province, Institutes of Physical Science and Information Technology, Anhui University, Hefei, Anhui, 230601, China
[13]Shanghai Key Laboratory of Atmospheric Particle Pollution and Prevention (LAP3), Department of Environmental Science and Engineering, Fudan University, Shanghai, 200433, China
[14]State Key Laboratory of Severe Weather & Institute of Tibetan Plateau Meteorology, Chinese Academy of Meteorological Sciences, Beijing, 100081, China
[15]Max Planck Institute for Chemistry, 55020, Mainz, Germany
[16]RT Solutions Inc., Cambridge, Massachusetts, 02138, USA
[17]College of Urban and Environmental Sciences, Peking University, Beijing, 100871, China
[18]R&D Satellite Observations Department, Royal Netherlands Meteorological Institute, De Bilt, the Netherlands

Correspondence to: Jintai Lin (linjt@pku.edu.cn)

Abstract

Tropospheric vertical column densities (VCDs) of nitrogen dioxide (NO_2) retrieved from sun-synchronous satellite instruments have provided abundant NO_2 data for environmental studies, but such

data are limited by retrieval uncertainties and insufficient temporal sampling (e.g., once a day). The Geostationary Environment Monitoring Spectrometer (GEMS) launched in February 2020 monitors NO_2 at an unprecedented hourly resolution during the daytime. Here we present a research product for tropospheric NO_2 VCDs, referred to as POMINO-GEMS. We develop a hybrid retrieval method combining GEMS, TROPOMI and GEOS-CF data to generate hourly tropospheric NO_2 slant column densities (SCDs). We then derive tropospheric NO_2 air mass factors (AMFs) with explicit corrections for surface reflectance anisotropy and aerosol optical effects, through parallelized pixel-by-pixel radiative transfer calculations. Prerequisite cloud parameters are retrieved with the O_2-O_2 algorithm by using ancillary parameters consistent with those used in NO_2 AMF calculations.

Initial retrieval of POMINO-GEMS tropospheric NO_2 VCDs for June–August 2021 exhibits strong hotspot signals over megacities and distinctive diurnal variations over polluted and clean areas. POMINO-GEMS NO_2 VCDs agree with the POMINO-TROPOMI v1.2.2 product (R = 0.98, and NMB = 4.9%) over East Asia, with slight differences associated with satellite viewing geometries and cloud and aerosol properties affecting the NO_2 retrieval. POMINO-GEMS also shows good agreement with OMNO2 v4 (R = 0.87, and NMB = −16.8%) and GOME-2 GDP 4.8 (R = 0.83, and NMB = −1.5%) NO_2 products. POMINO-GEMS shows small biases against ground-based MAX-DOAS NO_2 VCD data at nine sites (NMB = –11.1%) with modest or high correlation in diurnal variation at six urban and suburban sites (R from 0.60 to 0.96). The spatiotemporal variation of POMINO-GEMS correlates well with mobile-car MAX-DOAS measurements in the Three Rivers' Source region on the Tibetan Plateau (R = 0.81). Surface NO_2 concentrations estimated from POMINO-GEMS VCDs are consistent with measurements from the Ministry of Ecology and Environment of China for spatiotemporal variation (R = 0.78, and NMB = –26.3%) as well as diurnal variation at all, urban, suburban and rural sites ($R \geq 0.96$). POMINO-GEMS data will be made freely available for users to study the spatiotemporal variations, sources and impacts of NO_2.

1. Introduction

Tropospheric nitrogen dioxide (NO_2) is an important air pollutant. It ~~threats~~threatens human health, and contributes to the formation of tropospheric ozone (O_3) and nitrate aerosols (Crutzen, 1970; Shindell et al., 2009; Hoek et al., 2013; Chen et al., 2022). Satellite instruments provide observations of tropospheric NO_2 on a global scale, and they have been extensively used to estimate emissions of nitrogen

oxides (NO_x = NO + NO_2) (Lin and Mcelroy, 2011; Beirle et al., 2011; Gu et al., 2014; Kong et al., 2022a), surface NO_2 concentrations (Wei et al., 2022; Cooper et al., 2022), trends and variabilities (Richter et al., 2005; Cui et al., 2016; Krotkov et al., 2016; Van Der A et al., 2017), and impacts on human health and environment (Chen et al., 2021).

To date, most spaceborne instruments for NO_2 measurements, including the Global Ozone Monitoring Instrument (GOME) (Burrows, 1999), the Ozone Monitoring Instrument (OMI) (Levelt et al., 2006), the Global Ozone Monitoring Experiment 2 (GOME-2) (Callies et al., 2000) and the TROPOspheric Monitoring Instrument (TROPOMI) (Veefkind et al., 2012), are mounted on sun-synchronous low Earth orbit (LEO) satellites. These instruments passively measure backscattered radiance from the Earth's atmosphere, and measurements at each ground location are done 1–2 times a day. The Geostationary Environment Monitoring Spectrometer (GEMS) on board the Geostationary Korea Multi-Purpose Satellite-2B (GK-2B) was successfully launched in February 2020. The instrument provides measurements of NO_2 and other pollutants in the daytime on an hourly basis (Kim et al., 2020). It complements LEO satellite observations by providing a more comprehensive picture of the daytime evolution of NO_2.

There are three successive stages in the retrieval of tropospheric NO_2 vertical column densities (VCDs) in the UV-Vis range based on satellite observations. The first step is to retrieve total NO_2 slant column densities (SCDs) with spectral fitting techniques, such as the Differential Optical Absorption Spectroscopy (DOAS). The SCD represents the abundance of NO_2 along the effective light path from the sun through the atmosphere to the satellite instrument. Next, the contributions from stratospheric NO_2 to the total SCDs are removed in order to obtain tropospheric SCDs. Finally, the tropospheric SCDs are converted to VCDs using calculated air mass factors (AMFs). The AMF calculations are highly sensitive to the observation geometry, cloud parameters, aerosols, surface conditions and the shape of the NO_2 vertical distribution. Over polluted areas, errors in the retrieved tropospheric NO_2 VCDs are dominated by the uncertainties in AMF calculations (Boersma et al., 2004; Lorente et al., 2016) associated with aerosol optical effects, surface reflectance and a priori NO_2 vertical profiles (Zhou et al., 2010; Lin et al., 2014; Lin et al., 2015; Vasilkov et al., 2016; Lorente et al., 2018; Liu et al., 2019; Liu et al., 2020; Vasilkov et al., 2021).

The official GEMS retrieval algorithm for tropospheric NO_2 VCDs is developed by Lee et al. (2020).

The total NO_2 SCDs are retrieved using the DOAS technique. They are then converted to total NO_2 VCDs by using a precomputed look-up table of box AMFs based on the linearized pseudo-spherical scalar and vector discrete ordinate radiative transfer code (VLIDORT) version 2.6. Finally, stratosphere-troposphere separation (STS) is performed to derive tropospheric NO_2. Validation results have shown the overall capability of the official GEMS NO_2 algorithm (Kim et al., 2023), but several problems are also reported, such as overestimation of total NO_2 SCDs and tropospheric NO_2 VCDs, and some degree of striping in NO_2 retrieval data.

In this study, we present a research product which we name as POMINO-GEMS. This product is built upon our Peking University OMI NO_2 (POMINO) algorithm which focuses on the tropospheric AMF calculations and has been applied to OMI and TROPOMI (Lin et al., 2014; Lin et al., 2015; Liu et al., 2019; Liu et al., 2020; Zhang et al., 2022). Here we extend the AMF calculation by constructing a hybrid method to estimate tropospheric SCDs for GEMS. The hybrid method makes use of the total SCDs from the official GEMS product, total SCDs and stratospheric VCDs from the official TROPOMI product, as well as hourly stratospheric VCD data from the NASA Global Earth Observing System Composition Forecast (GEOS-CF) v1 product. We validate our initial set of retrieval results for tropospheric NO_2 VCDs in June-July-August (JJA) 2021, by using independent data of tropospheric NO_2 from the POMINO-TROPOMI v1.2.2, OMNO2 v4 and GOME-2 GDP 4.8 products, ground-based and mobile-car MAX-DOAS measurements, and surface concentration observations from the Ministry of Ecology and Environment (MEE) of China. We provide a simplified estimate of retrieval errors in the end.

2. Method and data

2.1 Construction of POMINO-GEMS retrieval algorithm

Figure 1 shows the flow chart of POMINO-GEMS retrieval algorithm. There are two essential steps. The first is to calculate tropospheric NO_2 SCDs on an hourly basis, through fusion of total SCDs from the official GEMS v1.0 L2 NO_2 product, total SCDs and stratospheric VCDs from the TROPOMI PAL v2.3.1 L2 NO_2 product, and diurnal variations of stratospheric NO_2 from the GEOS-CF v1 product. We then calculate tropospheric NO_2 AMFs to convert SCDs to VCDs.

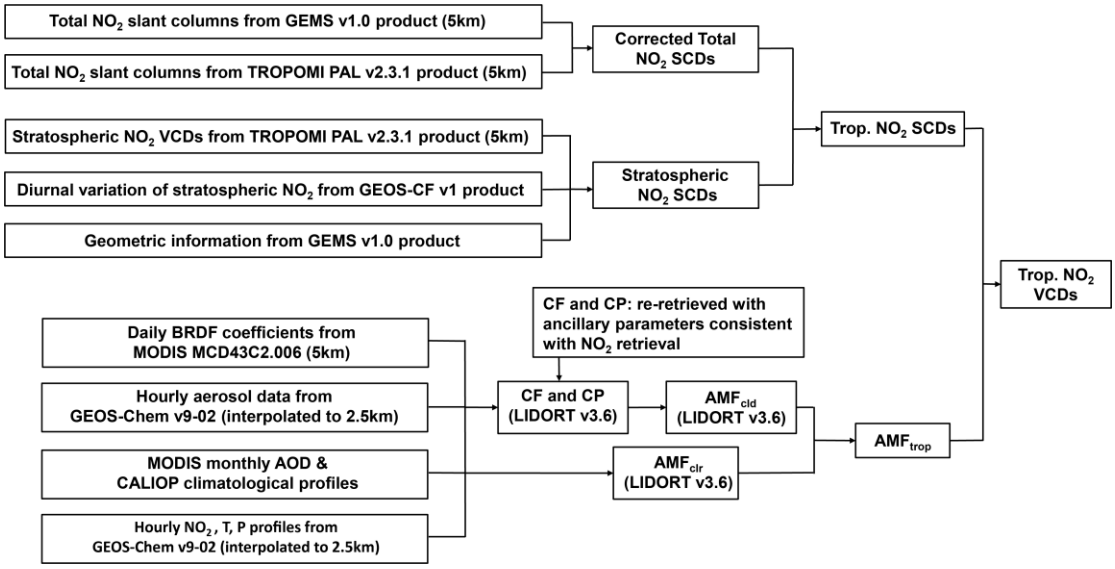

Figure 1. Flow chart of POMINO-GEMS retrieval algorithm. The numbers in the boxes, such as 5 km, refer to horizontal resolutions.

2.1.1 GEMS NO_2 and cloud data

The GEMS instrument is on board the GK-2B satellite locating at 128.2°E over the equator (Kim et al., 2020). The spectral wavelength range of GEMS is 300-500 nm, covering main absorption spectra of aerosols and trace gases. The nominal spatial resolution is typically 7 km × 8 km for gases and 3.5 km × 8 km for aerosols in the eastern and central scan domains; however, the north-south spatial resolution can exceed 25 km in the western side. The whole field of view (FOV) covers about 20 Asian countries within latitudes 5°S to 45°N and longitudes 80°E to 152°E. Given the variation of solar zenith angle (SZA), there are four scan scenarios moving from east to west, including Half East (HE), Half Korea (HK), Full Central (FC) and Full West (FW). It takes 30 minutes (for example, 00:45 – 01:15 UTC) for GEMS to scan its full coverage during each scenario, and the next 30 minutes to transmit data to the ground data center. The number of hourly GEMS observations per day varies from 6 in winter to 10 in summer, corresponding to the annual movement of subsolar points relative to the Earth.

We take hourly total (stratospheric + tropospheric) NO_2 SCDs from the official GEMS v1.0 L2 NO_2 product, and convert them to 0.05° × 0.05 ° gridded data by means of an area-weighted oversampling technique. The value of each grid cell is the mean value of pixel-based GEMS observations weighted by the ratio of the overlap area of each pixel to the area of grid cell. We also use continuum reflectance data (i.e., spectrally smooth reflectance from molecular and aerosol extinction as well as surface reflectance effects) and O_2-O_2 SCDs from the official GEMS v1.0 L2 cloud product to re-calculate cloud parameters

as a prerequisite for tropospheric NO_2 AMF calculations. Details of the GEMS retrievals can be found in the algorithm theoretical basis document (ATBD) (Lee et al., 2020).

2.1.2 TROPOMI, OMI and GOME-2 NO_2 data

Table S1 compares the basic information of GEMS with those of TROPOMI, OMI and GOME-2 instruments. In this study, TROPOMI data are used for derivation of POMINO-GEMS NO_2 VCDs, and data from all of the three LEO instruments are used for comparison with POMINO-GEMS.

We use total NO_2 SCDs and stratospheric NO_2 VCDs from the official TROPOMI PAL v2.3.1 L2 NO_2 product, and convert them to $0.05° \times 0.05°$ gridded data, again using an area-weighted oversampling technique. Details of TROPOMI total SCD retrievals and stratospheric VCD calculations are given in the TROPOMI ATBD (Van Geffen et al., 2022a). The TROPOMI PAL product is reprocessed with TROPOMI NO_2 data processor v2.3.1 for the period from 1 May 2018 to 14 November 2021; it will be replaced by the full mission reprocessing with NO_2 processor v2.4.0 in the future (Eskes et al., 2021). The most important improvement in this PAL product upon the previous OFFL v1.3 is the replacement of the FRESCO-S algorithm with the FRESCO-wide cloud retrieval algorithm, which leads to higher, more reasonable cloud pressure (CP) estimates and substantial increases in tropospheric NO_2 VCDs (by 20% – 50%) over polluted regions like Eastern China in winter (Eskes et al., 2021; Van Geffen et al., 2022b).

We use the POMINO-TROPOMI v1.2.2, OMNO2 v4 ~~(Krotkov et al., 2019)~~(Lamsal et al., 2021) and GOME-2 GDP 4.8 (Valks et al., 2019) tropospheric NO_2 VCD products to compare with POMINO-GEMS results. The previous POMINO-TROPOMI v1 data show higher accuracy in polluted situations and improved consistency with MAX-DOAS measurements when compared with the official TM5-MP-DOMINO (OFFLINE) product (Liu et al., 2020). POMINO-TROPOMI v1.2.2 improves upon v1 by (1) using tropospheric NO_2 SCD and CP data from the updated TROPOMI PAL v2.3.1 NO_2 product, (2) interpolating the daily NO_2, pressure, temperature and aerosol vertical profiles from nested GEOS-Chem (v9-02) simulations into a horizontal grid of 2.5 km x 2.5 km for subsequent tropospheric AMF calculations, and (3) including several minor bug fixes.

We select valid satellite pixels following common practice. For the daily POMINO-TROPOMI v1.2.2 L2 NO_2 product, we exclude pixels with SZA or viewing zenith angle (VZA) greater than 80°, high albedos caused by ice or snow on the ground, quality flag values (from the TROPOMI PAL v2.3.1

product) less than 0.5 or cloud radiance fraction (CRF) greater than 50%, and then map the valid data to a 0.05° × 0.05 °grid. For the daily OMNO2 v4 L2 NO_2 product, we exclude pixels with SZA or VZA greater than 80°, with scene Lambert-equivalent reflectivity (LER) greater than 0.3, affected by row anomaly (XTrackQualityFlags is not zero), marked without quality assurance (vcdQualityFlag is not an even integer) or with CRF greater than 50%, and then map the valid data to a 0.25° × 0.25 °grid. For the daily GOME-2 GDP 4.8 L2 NO_2 product, we exclude pixels with latitude greater than 70°, SZA greater than 80°, failed retrieval (NO2Tropo_Flag is set to 1 or 2) or with CRF greater than 50%, and then map the valid data to a 0.5° × 0.5° grid.

2.1.3 GEOS-CF stratospheric NO_2 data

The NASA GEOS-CF system combines the Global Earth Observing System (GEOS) weather analysis and forecasting system with GEOS-Chem v12.0.1 chemistry module (http://geoschem.org) to provide near real-time estimates of atmospheric compositions with daily 5-day forecasts. Detailed information of the model, including chemistry, emissions and deposition, and evaluation of the GEOS-CF tropospheric simulation and forecast skill are presented in Keller et al. (2021). In particular, the GEOS-Chem v12.0.1 chemistry scheme includes online stratospheric chemistry that is fully coupled with tropospheric chemistry through the Unified tropospheric-stratospheric Chemistry eXtension (UCX) mechanism (Eastham et al., 2014). The GEOS-CF stratospheric results are consistent with satellite observations, albeit with notable underestimation of NO_x and HNO_3 in the polar regions (Knowland et al., 2022b).

The GEOS-CF outputs have a horizontal resolution of 0.25° × 0.25 °and a temporal resolution of 1 hour for NO_2 and other ancillary data used here (Knowland et al., 2022a). We convert instantaneous stratospheric NO_2 volume mixing ratio in dry air at each hour (e.g., 00:00 UTC) into 0.05° × 0.05 ° gridded vertical column densities based on estimated tropopause information in GEOS-CF v1. In Section 2.1.5, we first evaluate GEOS-CF v1 stratospheric NO_2 VCDs with those of TROPOMI PAL v2.3.1 product, and then calculate hourly stratospheric NO_2 VCDs by combining GEOS-CF v1 data for each hour and TROPOMI PAL v2.3.1 stratospheric NO_2 VCD data in the early afternoon.

2.1.4 Calculation of total NO_2 SCDs

We use TROPOMI data to correct GEMS total NO_2 SCDs, given known issues in GEMS data. Specifics for the NO_2 SCD retrieval of TROPOMI PAL v2.3.1 and GEMS v1.0 operational products are

provided in Table S2.

Figure 2a and b show the spatial distribution of monthly mean total NO_2 geometric column densities (GCDs, calculated as SCDs divided by geometric AMFs) in June 2021 from TROPOMI PAL v2.3.1 and GEMS v1.0, respectively. The horizontal resolution is 0.05° × 0.05 °. The GCDs are used to compare the two products after removing the effect of measurement geometry. Matching for each day between hourly GEMS observations and the TROPOMI data at the closest observation time is done to ensure temporal compatibility. The figures show that the spatial pattern of GEMS GCDs agrees well with that of TROPOMI, with high values over the North China Plain (NCP) and Northwestern India, as well as major metropolitan clusters such as Seoul and the Yangtze River Delta (YRD). However, there are two systematic problems in GEMS GCDs. First, the GEMS GCD values are abnormally high over the northern and northwestern parts of GEMS FOV, especially over Mongolia, Qinghai, Inner Mongolia, Xinjiang and Tibet of China. Second, west-east stripes exist over the whole domain, similar to the spurious across-track variability issue for OMI. This stripe issue exists at all hours (Figure S1). It is likely associated with the specific scan modes of GEMS, as well as periodically occurring bad pixels as one of remaining calibration issues (Boersma et al., 2011; Lee et al., 2023).

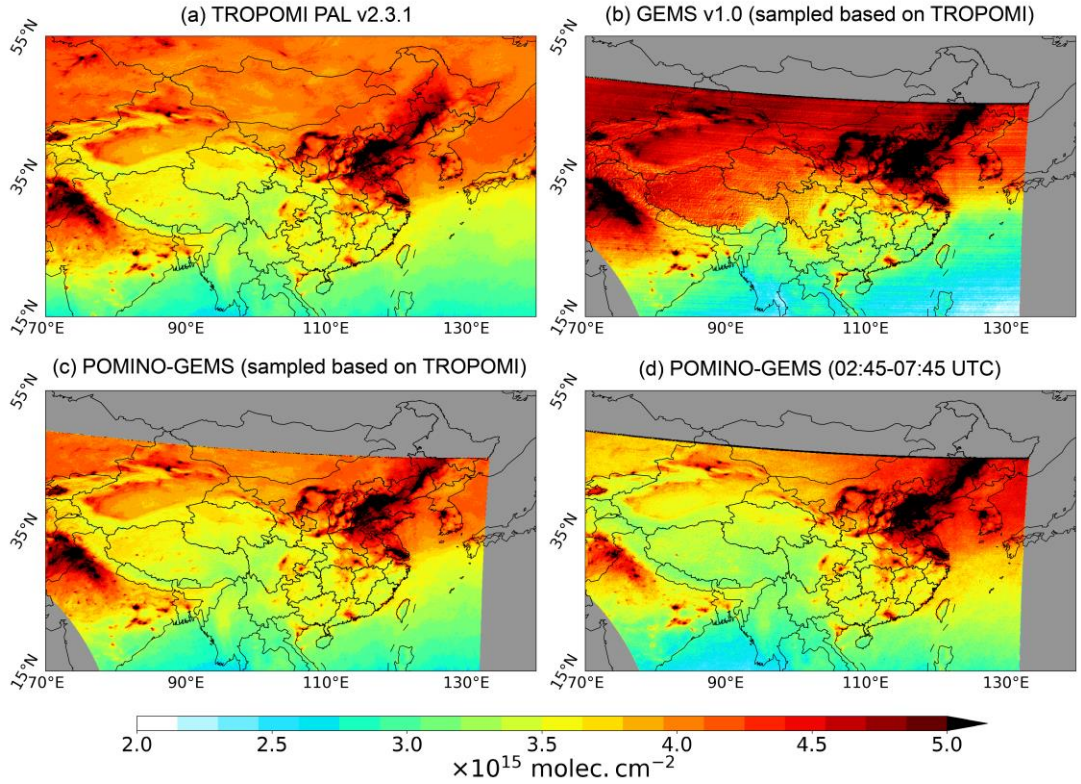

Figure 2. Spatial distribution of monthly mean total NO_2 GCDs on a 0.05° × 0.05 °grid in June 2021. (a) The TROPOMI PAL v2.3.1 product, (b) the official GEMS v1.0 product that spatiotemporally matches with TROPOMI, (c) the corrected POMINO-GEMS product that spatiotemporally matches with TROPOMI,

and (d) the corrected POMINO-GEMS product averaged over 02:45 – 07:45 UTC. Note the range of the color bar is 2.0 – 5.0 × 10^{15} molec. cm^{-2}. The regions in grey mean there are no valid observations.

To correct the two issues in the GEMS official total NO_2 SCD product, we combine GEMS and TROPOMI observations to obtain hourly 0.05° × 0.05 °corrected total NO_2 SCDs for each day using Eqs. (1) and (2):

$$\Delta\mathrm{GCD} = \frac{1}{n}\sum_{i=1}^{n}(\mathrm{GCD}_{\mathrm{total},h_i}^{\mathrm{TROPOMI}} - \mathrm{GCD}_{\mathrm{total},h_i}^{\mathrm{GEMS}}) \quad (1)$$

$$\mathrm{SCD}_{\mathrm{total},h}^{\mathrm{corrected}} = \mathrm{SCD}_{\mathrm{total},h}^{\mathrm{GEMS}} + \Delta\mathrm{GCD} \times \mathrm{AMFgeo}_{h}^{\mathrm{GEMS}} \quad (2)$$

In Eqs. (1) and (2), index h represents the hour of GEMS observations on each day; h_i the hour when both GEMS and TROPOMI have valid observations for the same grid cell; and n the number of h_i. The value of n is 1 or 2 depending on the overpass times of TROPOMI. There are two steps in the correction process. First, we calculate a geometry-independent correction map for each day using total NO_2 GCDs from GEMS and TROPOMI that match spatially and temporally (Eq. (1)). We use the absolute difference instead of a scaling factor as a simple correction. We then apply the correction to the original GEMS total NO_2 SCDs at each hour on the same day, with the diurnal variation in AMF associated with measurement geometry accounted for (Eq. (2)).

In Eq. (2), we implement a simple geometric correction (concerning SZAs and VZAs) for AMFs instead of using the actual AMFs; the latter could account for the differences in relative azimuth angles and other factors. Specific derivation of this assumption is given in Section 1 of the Supplement Information (SI). The correction is assumed to be acceptable with an extra uncertainty introduced to the total NO_2 SCDs, as will be further discussed in Section 3.5.

Figure 2c shows the monthly mean corrected POMINO-GEMS total NO_2 GCDs in June 2021 after spatial and temporal matching with TROPOMI. The corrected GCD values in the northern GEMS FOV are much reduced compared with those in the original GEMS data. Moreover, most stripe-like patterns are removed in the corrected GCDs. Figure 2d is similar to Fig. 2c but for GCDs averaged over 02:45 – 07:45 UTC in June 2021. Figure S3 further compares the original GEMS and POMINO-GEMS total NO_2 GCDs at each hour in JJA 2021, showing similar improvements as well. The differences between Figure 2c and d indicate the influence of different sampling hours combined with the daily correction map. Specifically, the correction value of each grid cell is calculated at the specific hour when both GEMS and TROPOMI have valid observations, but this value is applied to original GEMS SCDs at all

hours.

Our correction method is done for each grid cell. We tested other correction methods by applying the same correction value to grid cells within a 20° × 20 °domain, at the same latitude, or at the same longitude. These alternative methods can reduce the high bias over the northern and northwestern GEMS FOV to various extents, but cannot remove the stripes (not shown). We also note that our simple correction is a temporary solution before the aforementioned systematic problems in the official GEMS SCD retrieval are solved by improving spectral fitting. In Sections 3.3 and 3.4, we compare the diurnal variations of tropospheric NO_2 VCDs based on corrected and uncorrected GEMS SCDs.

2.1.5 Calculation of stratospheric and tropospheric NO_2 SCDs

We construct a dataset of hourly stratospheric NO_2 SCDs at 0.05° × 0.05 °by using TROPOMI PAL v2.3.1 stratospheric NO_2 VCDs, diurnal variation of stratospheric NO_2 VCDs provided by GEOS-CF v1 product, and GEMS geometric AMFs.

Figure S4 shows the comparison results between GEOS-CF v1 and TROPOMI PAL v2.3.1 stratospheric NO_2 VCDs in June 2021. Consistent spatial and temporal sampling is done. N is the total number of matched 0.05° × 0.05 °grid cells. The stratospheric VCDs from both products vary in the range of 2 – 5 × 10^{15} molec. cm^{-2}, with spatiotemporal correlation of 0.99, linear regression slope of 0.99 and normalized mean bias (NMB) of 0.02%. This consistency provides confidence on the overall reliability of GEOS-CF stratospheric NO_2 data.

First, we calculate stratospheric NO_2 VCDs at a reference hour for each day using Eqs. (3) and (4):

$$\mathrm{ratio}_{h_0}^{h} = \frac{\mathrm{VCD}_{\mathrm{strat},h}^{\mathrm{GEOS-CF}}}{\mathrm{VCD}_{\mathrm{strat},h_0}^{\mathrm{GEOS-CF}}} \quad (3)$$

$$\mathrm{VCD}_{\mathrm{strat},h_0} = \frac{1}{\mathrm{n}}\sum_{\mathrm{i=1}}^{\mathrm{n}} \frac{\mathrm{VCD}_{\mathrm{strat},h_i}^{\mathrm{TROPOMI}}}{\mathrm{ratio}_{h_0}^{h_i}} \quad (4)$$

Here, Eq. (3) defines the ratio of GEOS-CF stratospheric NO_2 at hour h to that at the reference hour h_0, which is chosen to be 01:00 UTC (Figure S5). In Eq. (4), h_i represents the observation time of every TROPOMI orbit that overlaps with GEMS FOV, and n the number of h_i for each grid cell.

Second, we use the ratio from a given time h to h_0 and stratospheric NO_2 VCDs at h_0 to derive stratospheric NO_2 VCDs at h for each day (Eq. (5)).

$$\mathrm{VCD}_{\mathrm{strat},h} = \mathrm{VCD}_{\mathrm{strat},h_0} \times \mathrm{ratio}_{h_0}^{h} \quad (5)$$

Figure 3 shows the derived monthly mean stratospheric NO_2 VCDs at each hour in June 2021 on a

0.05° × 0.05 °grid. The abrupt decease of stratospheric NO_2 VCDs after sunrise is caused by resumed photochemical conversion of NO_2 to NO (Li et al., 2021b). There is a strong meridional gradient of stratospheric NO_2 in the daytime, with the higher values in the north associated with longer lifetimes. The stratospheric NO_2 increase quasi-linearly during the daytime; linear regression to the mean stratospheric NO_2 VCDs over the whole domain from 01:45 to 07:45 UTC results in an increasing rate of (1.12±0.03) × 10^{14} molec. cm^{-2} h^{-1}. This result is consistent with previous work showing quasi-linear growth in the daytime at rates of 0.5 – 2 × 10^{14} molec. cm^{-2} h^{-1} depending on latitude and season (Li et al., 2021b; Dirksen et al., 2011).

Finally, we use GEMS geometric AMFs to convert the stratospheric NO_2 VCDs to SCDs at each hour, and then subtract them from the total SCDs to obtain tropospheric SCDs (Eqs. (6) and (7)). In the stratosphere, the geometric AMFs are essentially the same as the actual AMFs

$$\mathrm{SCD}_{\mathrm{strat},h} = \mathrm{VCD}_{\mathrm{strat},h} \times \mathrm{AMFgeo}_{h}^{\mathrm{GEMS}} \quad (6)$$

$$\mathrm{SCD}_{\mathrm{trop},h}^{\mathrm{GEMS}*} = \mathrm{SCD}_{\mathrm{total},h}^{\mathrm{corrected}} - \mathrm{SCD}_{\mathrm{strat},h} \quad (7)$$

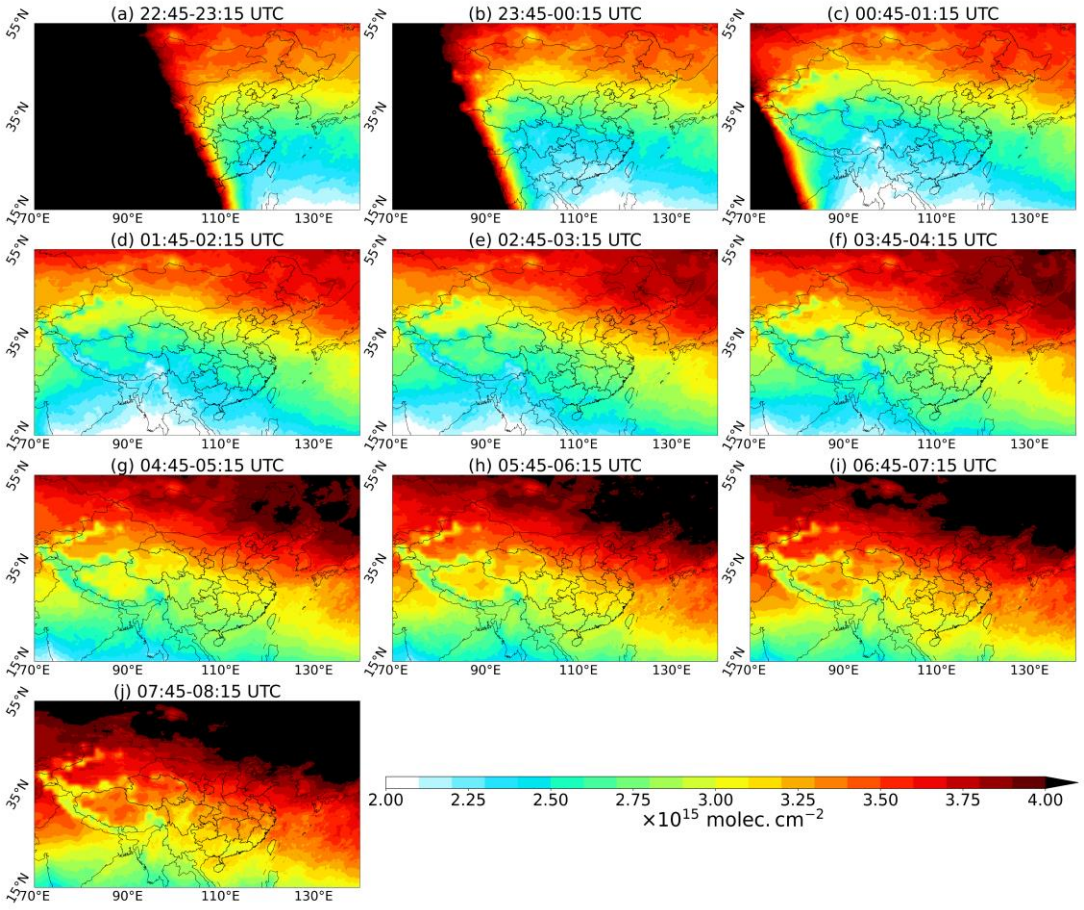

Figure 3. Spatial distribution of POMINO-GEMS derived monthly mean stratospheric NO_2 VCDs at each hour on a 0.05° × 0.05 °grid in June 2021. Note the range of the color bar is 2.0 – 4.0 × 10^{15} molec. cm^{-2}.

2.1.6 Calculation of tropospheric AMFs

Tropospheric NO_2 AMF is dependent on three factors as defined in Palmer et al. (2001): the viewing geometry, the scattering weights describing the sensitivity of the backscattered spectrum to the abundance of the absorber, and a priori NO_2 vertical profile (Eq. (8)).

$$\mathrm{AMF} = \mathrm{AMF_G} \int_0^{z_\mathrm{T}} w(z) S(z) \mathrm{d}z \tag{8}$$

In Eq. (8), $\mathrm{AMF_G}$ is the geometric AMF and a function of SZA and VZA, $w(z)$ the scattering weight at altitude z, $S(z)$ the normalized vertical profile of NO_2 number density, and z_T the tropopause. Following Yang et al. (2023), we refer to $\int_0^{z_\mathrm{T}} w(z) S(z) \mathrm{d}z$ as the scattering correction factor for discussion in Section 3.2. For tropospheric AMF calculations (Figure 1), we use a parallelized AMFv6 package driven by LIDORT version 3.6; this is similar to the one used in our previous POMINO products (Lin et al., 2014; Lin et al., 2015; Liu et al., 2019) but with modifications to adapt to the geostationary observing characteristics and high spatiotemporal resolution of GEMS. We take daily BRDF coefficients with a horizontal resolution of 5 km from the MODIS MCD43C2.006 dataset (Lucht et al., 2000) to account for the anisotropy of surface reflectance over land and coastal ocean regions , and OMLER v3 albedo over open ocean (Zhou et al., 2010; Lin et al., 2014; Liu et al., 2020). Hourly-varying aerosol parameters, a priori NO_2 profiles, temperature profiles and pressure profiles are interpolated from nested GEOS-Chem (v9-02) results to a horizontal resolution of 2.5 km, using the Piecewise Cubic Hermite Interpolating Polynomial (PCHIP) method. Furthermore, we deploy AOD observations from the MODIS/Aqua Collection 6.1 MYD04_L2 dataset to constrain model-simulated AOD on a monthly basis (Lin et al., 2014; Lin et al., 2015; Liu et al., 2019; Liu et al., 2020); and we use a self-constructed monthly climatological dataset of aerosol extinction profiles based on CALIOP L2 data over 2007-2015 to constrain modeled aerosol vertical profiles on a monthly climatology basis (Liu et al., 2019). We re-retrieve cloud parameters based on O_2-O_2 SCDs and continuum reflectances from the official GEMS v1.0 cloud product, using ancillary parameters consistent with those used in NO_2 AMF calculations. Instead of relying on a look-up table (LUT), we conduct pixel-by-pixel radiative transfer calculations with the parallelized AMFv6 package. The independent pixel approximation (IPA) is assumed for cloud-contaminated pixels as in other algorithms. Finally, we use the AMF data to convert tropospheric NO_2 SCDs to VCDs.

Invalid pixels in the POMINO-GEMS product are filtered based on the following criteria. We

exclude pixels with SZA or VZA greater than 80°, or with the ground covered by ice or snow. To minimize cloud contamination, we exclude pixels with CRF greater than 50%.

2.2 Estimation of surface NO_2 concentrations

In order to validate satellite NO_2 products with surface concentration measurements from MEE, we convert tropospheric NO_2 VCDs from satellite products on a $0.05° \times 0.05°$ grid to surface NO_2 mass concentrations using GEOS-Chem simulated NO_2 vertical profiles and the box heights of the lowest model layer (Eq. (9)).

$$C_{\text{surf}} = \text{VCD}_{\text{trop}}^{\text{SAT}} \times R^{\text{GC}} \times \frac{M}{N \times H^{\text{GC}}} \times 2 \quad (9)$$

In Eq. (9), C_{surf} represents the estimated surface NO_2 mass concentration in μg m^{-3}, $\text{VCD}_{\text{trop}}^{\text{SAT}}$ the satellite tropospheric VCD in molecules. m^{-2}, R^{GC} the GEOS-Chem simulated hourly ratio of NO_2 sub-column in the lowest layer to the total tropospheric column, M the NO_2 molar mass in μg mol^{-1}, N the Avogadro constant, and H^{GC} the box height of the lowest layer in m. The thickness of the lowest layer of GEOS-Chem (about 130 m) is too large for the layer average NO_2 mass concentration to represent that near the ground (Liu et al., 2018a); thus the derived concentration is multiplied by a factor of 2 to roughly account for the vertical gradient from the height of ground instrument to the center of the model layer. However, the constant correction factor of 2 neglects the diurnal variation of NO_2 vertical gradient, which is related to the diurnal variation of planetary boundary layer (PBL) heights. This issue is discussed in detail in Section 3.4.

2.3 Ground-based MAX-DOAS measurements

We use ground-based MAX-DOAS NO_2 measurements, together with POMINO-TROPOMI v1.2.2, OMNO2 v4 and GOME-2 GDP 4.8 NO_2 products, to validate the POMINO-GEMS retrieval results. The types, geolocations and observation times of MAX-DOAS stations are summarized in Table S3, and the location of each site is shown in Figure S6. Details of each site are described in Section 2 of the SI. Kanaya et al. (2014) and Hendrick et al. (2014) have discussed the error in MAX-DOAS NO_2 retrieval: uncertainties from a priori aerosol and NO_2 profiles are the largest source by 10% – 14%, and the total retrieval uncertainty is typically 12% – 17%.

To ensure sampling consistency in time, we average all valid MAX-DOAS measurements within each observation period of GEMS (i.e., 30 minutes) for hourly comparison, and within $\pm$1.5 h of

TROPOMI, OMI and GOME-2 overpass time for daily comparison. Following the procedures in previous studies (Lin et al., 2014; Liu et al., 2020), we exclude all matched MAX-DOAS data for which the standard deviation exceeds 20% of the mean value to minimize the influence of local events. To ensure sampling consistency in space, we select valid satellite pixels within 5 km of MAX-DOAS sites for POMINO-GEMS and POMINO-TROPOMI v1.2.2, 25 km for OMNO2 v4 and 50 km for GOME-2 GDP 4.8, and conduct spatial averaging. The Grubbs statistical test, which is used to detect outliers in a univariate data set assumed to exhibit normal distribution (Grubbs, 1950), is performed to exclude outliers in both MAX-DOAS and satellite data before comparison. Only one data pair from Fudan University site is identified as an outlier and removed (Figure S7), and we get 1348 matched hourly data pairs in total.

2.4 Mobile-car MAX-DOAS measurements

We use tropospheric NO_2 VCDs from mobile-car MAX-DOAS measurements performed by the Chinese Academy of Meteorological Sciences (CAMS) in the Three Rivers' Source region in July 2021 (Cheng et al., 2023). The Three Rivers' Source region is on the northeastern Tibetan Plateau in western China, which is isolated from massive anthropogenic activities, and hence a good place for observations of atmospheric compositions in the background atmosphere. The field campaign lasted from 18th to 30th July 2021 and included four closed-loop journeys, beginning from the meteorological bureau of the city of Xining (the Capital of Qinghai Province) to the meteorological bureau of Dari County of the Guoluo Tibetan Autonomous Prefecture, to the meteorological bureau of Yushu Tibetan Autonomous Prefecture, and then back to Xining City (Figure S6). The spectral analysis of the measurement spectra in the fitting window of 400-434 nm was implemented with the DOAS method. Sequential Fraunhofer reference spectrum (FRS) is used to derive NO_2 differential slant column densities (DSCDs), which are then converted to VCDs by adopting the geometric approximation method. The errors are estimated to be less than 20% at high altitudes. More detailed descriptions of instrumentation, field campaign and data retrieval are in Cheng et al. (2023).

We average all valid mobile-car MAX-DOAS measurements within each observation period of GEMS in each 0.05° × 0.05 °grid cell, to ensure spatiotemporal consistency. Over relatively clean areas with little human influence and biomass burning such as the Three Rivers' Source region, a large portion of NO_2 is located in the middle and upper troposphere, which is not accounted for in the mobile-car data

via such a DSCD-based retrieval method. Indeed, Cheng et al. (2023) showed that the official TROPOMI NO_2 VCDs are higher than mobile-car data by about 40%. Considering that the diurnal variation of middle and upper tropospheric NO_2 is much smaller than that in the lower troposphere, we focus on the correlation of NO_2 diurnal variation between POMINO-GEMS and mobile car MAX-DOAS data.

2.5 Ground-based MEE NO_2 measurements

We use hourly surface NO_2 mass concentration measurements from the MEE air quality monitoring network. By 2021, more than 2000 MEE stations across China have been established, providing hourly observations for NO_2 and five other air pollutants. Most stations are in urban or suburban areas.

The spatial distribution of all MEE sites in the GEMS FOV is shown in Figure S8a, and that of MEE sites over urban, suburban and rural regions are shown in Figure S8b–d, respectively. The classification of sites is based on Tencent user location data with a horizontal resolution of 0.05° × 0.05 °for every 0.5 second from 31 August to 30 September 2021 (Figure S8e), adopted from previous work (Kong et al., 2022a). Here, urban MEE sites are defined as where the mean location request times is larger than 50 times per second, suburban sites refer to 5-50 times per second, and rural sites refer to less than 5 times per second. The number of sites for urban, suburban and rural sites are 808, 554 and 71, respectively.

At MEE sites, molybdenum catalyzed conversion from NO_2 to NO and subsequent chemiluminescence measurement of NO is done to estimate NO_2 concentrations. The heated molybdenum catalyst has low chemical selectivity, leading to strong interference from other oxidized nitrogen species such as nitric acid (HNO_3) and peroxyacetyl nitrate (PAN). Therefore, MEE data tend to overestimate the actual NO_2 concentrations, with the extent of overestimation about 10% – 50% (Boersma et al., 2009; Liu et al., 2018a). The overestimation is dependent on the oxidation level of NO_x, but is currently unclear for each site and hour.

To compare with satellite-derived surface NO_2 concentration data, we average over all valid MEE sites in each 0.05° × 0.05 °grid cell to generate gridded MEE NO_2 data for each hour. To ensure sampling consistency for each day, we average MEE observations at two consecutive hours to match GEMS hourly observations – for example, we match the mean value of MEE NO_2 concentrations in 13:00 – 14:00 and 14:00 – 15:00 local solar time (LST) with the GEMS NO_2 in 13:45 – 14:15 LST. We also match MEE observations over the period 13:00 – 14:00 LST with TROPOMI-derived and OMI-derived surface NO_2, and 9:00 – 10:00 LST with GOME-2-derived surface NO_2.

3. Results and discussion

3.1 POMINO-GEMS tropospheric NO_2 VCDs

Figure 4 shows mean POMINO-GEMS tropospheric NO_2 VCDs at each hour on a 0.05° × 0.05 ° grid in JJA 2021. High values of tropospheric NO_2 columns (> 10×10^{15} molec. cm^{-2}) are evident over populous regions such as South Korea, central and eastern China, and northern India. Clear hotspot signals reveal intense NO_x emissions over city clusters such as Beijing-Tianjin-Hebei (BTH), Yangtze River Delta (YRD), Pearl River Delta (PRD) and Seoul Metropolitan Area (SMA), as well as isolated megacities such as Osaka and Nagoya in Japan, Chengdu and Urumqi in China, and New Delhi in India. Tropospheric NO_2 VCDs are much lower (< 1×10^{15} molec. cm^{-2}) over most of western China and the open ocean, due to low anthropogenic and natural emissions.

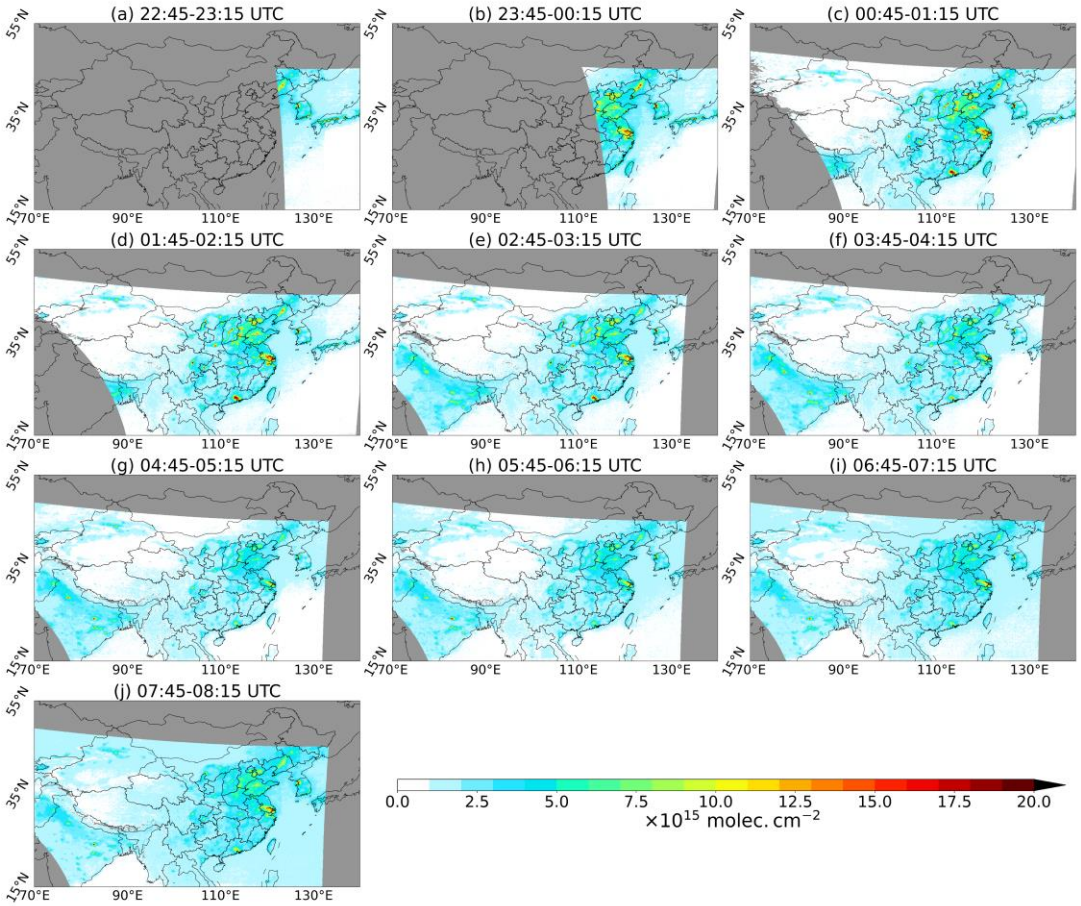

Figure 4. Spatial distribution of POMINO-GEMS tropospheric NO_2 VCDs at each hour on a 0.05° × 0.05 ° grid in JJA 2021. The regions in grey mean there are no valid observations.

Figure 5a-c present NO_2 VCDs in the morning, noon and afternoon in JJA 2021 for eastern China. Data are averaged in 22:45 – 01:45 UTC (06:45 – 09:45 Beijing Time, BJT), 02:45 – 04:45 UTC (10:45

– 12:45 BJT) and 05:45 – 07:45 UTC (13:45 – 15:45 BJT) to represent the morning, noon and afternoon, respectively. In the morning (Figure 5a), there are clear city signals with high NO_2 values, reflecting abundant NO_x emissions from traffic. The spatial gradients of NO_2 from urban centers to outskirts are very strong. However, these spatial gradients are greatly reduced in the noon and afternoon (Figure 5b and c). For example, the differences of tropospheric NO_2 VCDs between the urban center of Xi'an (108.93°N, 34.27°E) and its surrounding areas (within 50 km) are reduced from about 8×10^{15} molec. cm^{-2} in the morning to about 4×10^{15} molec. cm^{-2} at noon, and then to below 2×10^{15} molec. cm^{-2} in the afternoon. This is likely due to chemical loss of traffic-associated NO_2, increased emissions from other sectors (e.g., industry), and/or enhanced horizontal transport smearing the spatial gradient.

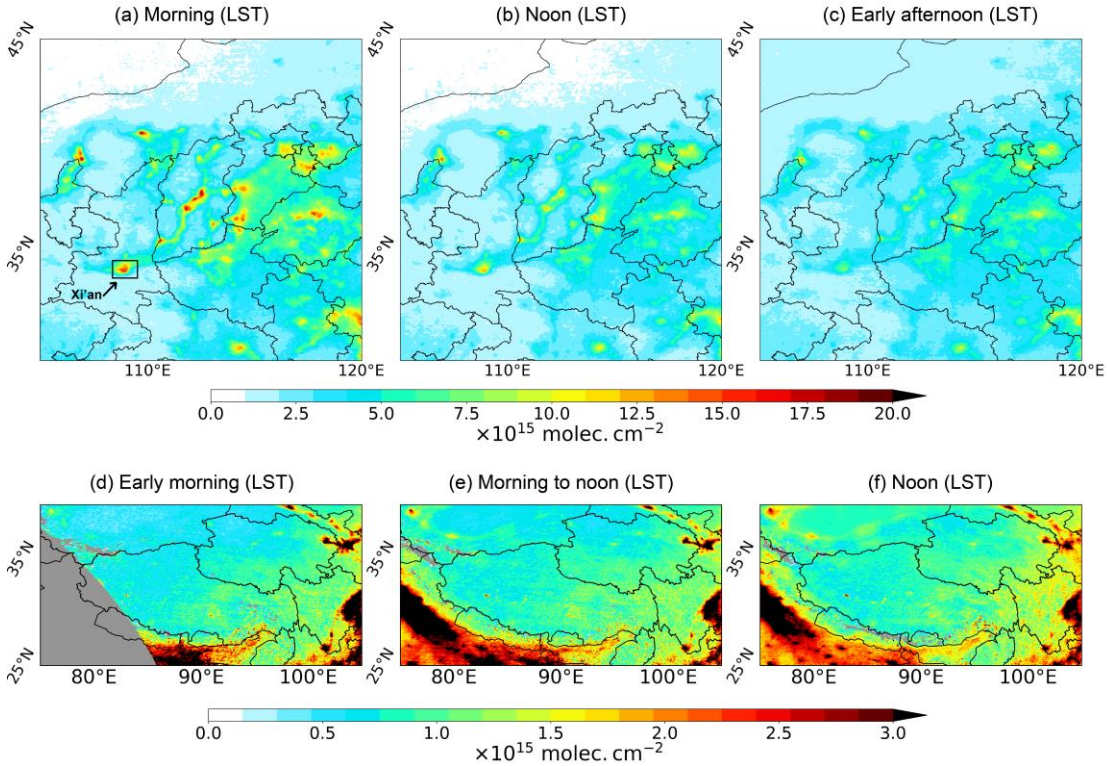

Figure 5. Spatial distribution of three-hour-mean POMINO-GEMS tropospheric NO_2 VCDs in JJA 2021 on a 0.05° × 0.05 °grid. The first row is for eastern China in the (a) morning (22:45 – 01:45 UTC), (b) noon (02:45 – 04:45 UTC) and (c) afternoon (05:45 – 07:45 UTC). The second row is for western China in the (d) early morning (00:45 – 01:45 UTC), (e) morning to noon (02:45 – 04:45 UTC) and (f) noon (05:45 – 07:45 UTC). The regions in grey mean there are no valid observations.

Over western China with low tropospheric NO_2 VCDs (Figure 5d-f), there is a gradual increase of tropospheric NO_2 by about 1×10^{15} molec. cm^{-2} from the early morning to noon. This increase is likely dominated by biogenic NO_x emissions that are sensitive to sunshine intensity and surface temperature (Kong et al., 2022b; Weng et al., 2020; Kong et al., 2023). Future studies are needed to understand the

exact causes.

Figure 6 shows the diurnal variation of POMINO-GEMS tropospheric NO_2 VCDs over six different region groups in the GEMS FOV. The six groups are defined based on the levels of mean POMINO-GEMS tropospheric NO_2 VCDs at 12:00 LST in JJA 2021 ($VCD_{12:00\ LST}$), and their spatial distributions are also shown in each panel. We convert the observation time from UTC to LST for each time zone in this domain (+5 time zone: 70°E – 82.5° E; +6 time zone: 82.5°E – 97.5°E; +7 time zone: 97.5°E – 112.5°E; +8 time zone: 112.5°E – 127.5°E; +9 time zone: 127.5°E – 140°E), and show the NO_2 diurnal variations in each time zone with different colors. For low NO_2 situations ($VCD_{12:00\ LST} \leq 2 \times 10^{15}$ molec. cm^{-2}), NO_2 grow in the morning time in +5 and +6 time zones but not in other time zones. Over high NO_2 situations ($VCD_{12:00\ LST} > 8 \times 10^{15}$ molec. cm^{-2}, in cities and suburban areas), NO_2 in all time zones exhibit a minimum around noontime and a morning peak at 09:00 – 10:00 LST, consistent with previous findings for specific polluted locations (Boersma et al., 2008; Boersma et al., 2009; Li et al., 2021a; Ghude et al., 2020; Herman et al., 2019; Biswas and Mahajan, 2021). In all groups and time zones, tropospheric NO_2 VCDs grow from noon to the afternoon.

The NO_2 diurnal variations are related to multiple driving factors. Different sources with distinctive diurnal patterns dominate the NO_x emissions over different regions. Lightning and biogenic activities are the major emission sources over low NO_2 land areas, and they tend to intensify with temperature and radiation in the daytime. Anthropogenic emissions are dominant over polluted cities and suburban areas, where the traffic emissions tend to peak in the mid-morning and late afternoon (Jing et al., 2016; Liu et al., 2018b; Naiudomthum et al., 2022). In addition, the photochemistry plays an important role. NO_2 is in chemical balance with NO, and the ratio of NO_2 and NO depends on radiation, ozone and peroxyl radicals. NO_x is oxidized to nitric acid and organic nitrates by radicals in the daytime, the level of which depends on radiation, ozone and volatile organic compounds. Thus the lifetime of NO_2 reaches the minimum value around noon, i.e., a few hours in summer. Furthermore, atmospheric transport also affects the diurnal variation of NO_2 at high-value places (e.g., cities) and their surroundings. Further studies are needed to determine the exact causes of NO_2 diurnal variations at individual places.

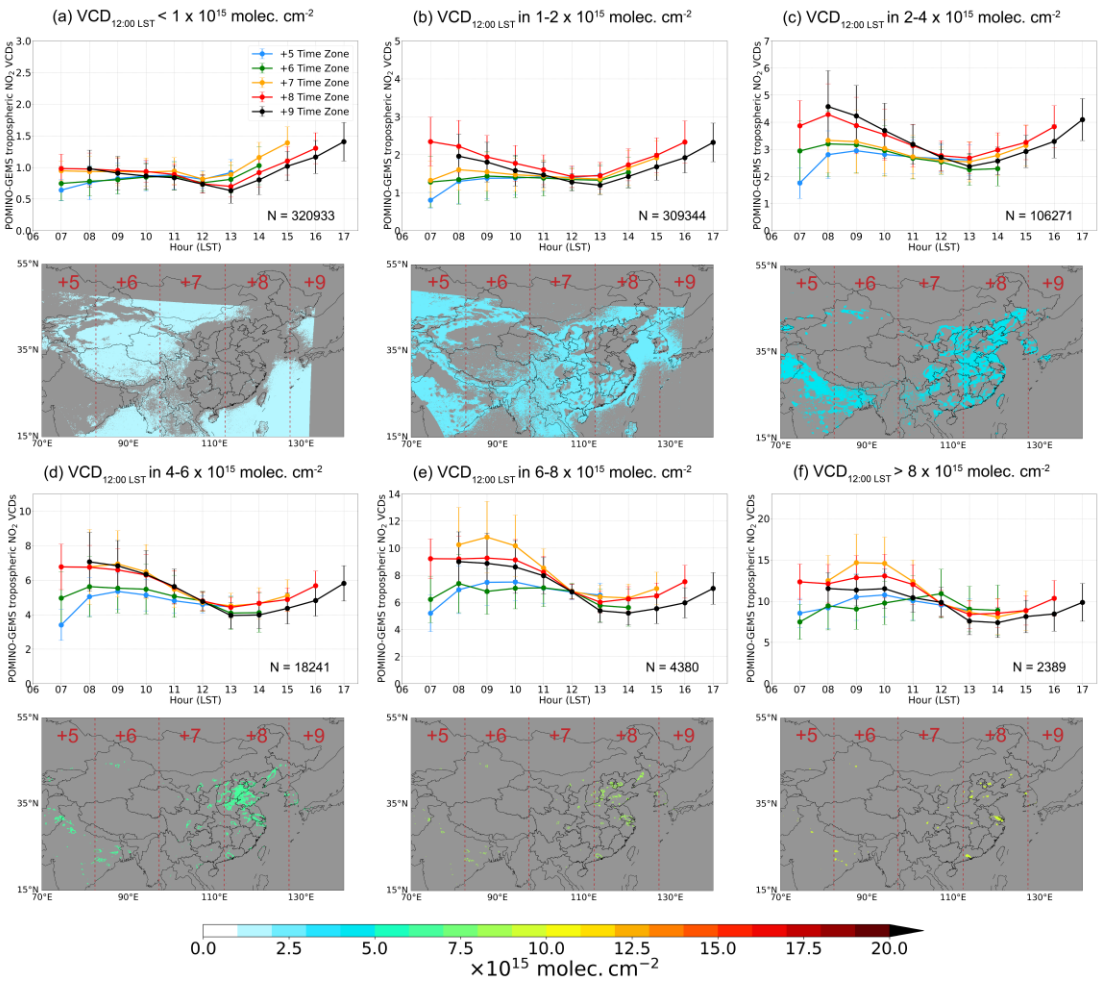

Figure 6. POMINO-GEMS NO_2 diurnal variations for six region groups classified based on mean POMINO-GEMS tropospheric NO_2 VCDs at 12:00 LST in JJA 2021 ($VCD_{12:00\ LST}$). (a) $VCD_{12:00\ LST}$ less than 1×10^{15} molec. cm^{-2}; (b) $VCD_{12:00\ LST}$ in $1 - 2 \times 10^{15}$ molec. cm^{-2}; (c) $VCD_{12:00\ LST}$ in $2 - 4 \times 10^{15}$ molec. cm^{-2}; (d) $VCD_{12:00\ LST}$ in $4 - 6 \times 10^{15}$ molec. cm^{-2}; (e) $VCD_{12:00\ LST}$ in $6 - 8 \times 10^{15}$ molec. cm^{-2} and (f) $VCD_{12:00\ LST}$ larger than 8×10^{15} molec. cm^{-2}. In each panel, different colors denote the NO_2 diurnal variation in different time zones. N denotes the total number of valid 0.05° × 0.05° grid cells in each region. The error bars denote the standard deviation of tropospheric NO_2 VCDs at each hour in each time zone.

3.2 Comparison with POMINO-TROPOMI v1.2.2, OMNO2 v4 and GOME-2 GDP 4.8 NO_2 VCD products

Figure 7a and b show the POMINO-GEMS and POMINO-TROPOMI v1.2.2 tropospheric NO_2 VCDs, respectively, on a 0.05° × 0.05 °grid averaged over JJA 2021. Cloud screening is implemented based on the CRFs from each product. To ensure temporal compatibility, matching between hourly GEMS observations and the TROPOMI data at the closest observation time is done for each day. Overall, POMINO-GEMS agrees well with POMINO-TROPOMI with a spatial correlation coefficient of 0.98, a linear regression slope of 1.18 and a small positive NMB of 4.9% (Figure 7c). Regionally, POMINO-

GEMS VCDs are higher than those of POMINO-TROPOMI v1.2.2 over eastern China, most India and northwestern GEMS FOV, but smaller over western China and the oceans (Figure 7a, b; see Figure S9c and d for differences plots). These differences are related to tropospheric NO_2 AMFs and SCDs. Detailed discussion is given in Section 3 of the SI.

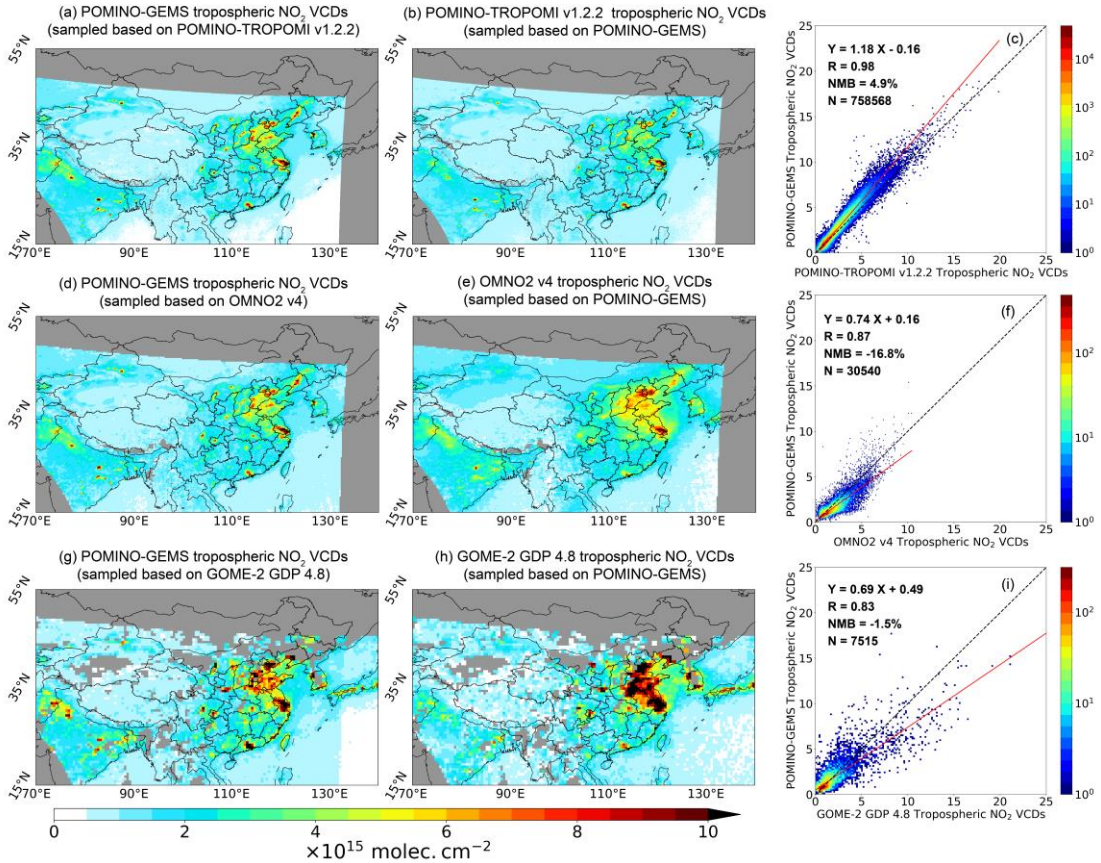

Figure 7. Comparison between POMINO-GEMS and other products for tropospheric NO_2 VCDs in JJA 2021. (a-b) Between POMINO-GEMS and POMINO-TROPOMI v1.2.2 on a 0.05° × 0.05 °grid, (d-e) between POMINO-GEMS and OMNO2 v4 on a 0.25° × 0.25 °grid, and (g-h) between POMINO-GEMS and GOME-2 GDP 4.8 on a 0.5° × 0.5 °grid. (c), (f) and (i) are respective scatterplots, in which the colors represent data density. The regions in grey mean there are no valid observations.

Figure 7d-f and g-i show the comparison results of POMINO-GEMS tropospheric NO_2 VCDs with OMNO2 v4 on a 0.25° × 0.25° grid and GOME-2 GDP 4.8 on a 0.5° × 0.5 °grid averaged over JJA 2021, respectively. POMINO-GEMS NO_2 VCDs exhibit good spatial consistency with the two independent products (R = 0.87 and 0.83), although with slightly lower values than OMNO2 v4 (by 16.8%) and GOME-2 GDP 4.8 (by 1.5%). These VCD differences are expected, considering the differences in the retrieval algorithm. For example, the POMINO-GEMS algorithm implements explicit aerosol corrections in the radiative transfer calculation, while OMNO2 v4 and GOME-2 GDP 4.8 treat aerosols as "effective clouds". POMINO-GEMS accounts for the anisotropy of surface reflectance by adopting

MODIS BRDF coefficients, whereas OMNO2 v4 and GOME-2 GDP 4.8 use geometry-dependent and regular LER, respectively. The horizontal resolution of a priori NO_2 profiles in POMINO-GEMS is 25 km (and interpolated to 2.5 km), 1° × 1.25 °in OMNO2 v4 and 1.875° × 1.875 °in GOME-2 GDP 4.8 ~~(Krotkov et al., 2019; Valks, 2019).~~(Valks, 2019; Lamsal et al., 2021).

Based on comparisons with POMINO-TROPOMI v1.2.2, OMNO2 v4 and GOME-2 GDP 4.8 NO_2 VCDs, we conclude that POMINO-GEMS NO_2 columns show good agreement with LEO satellite data, with lower values by 20% at most.

3.3 Validation with MAX-DOAS NO_2 VCD measurements

The scatterplot in Figure 8a compares POMINO-GEMS tropospheric NO_2 VCDs in JJA 2021 at all GEMS observation hours with matched ground based MAX-DOAS measurements at nine sites. POMINO-GEMS correlates with MAX-DOAS (R = 0.66) with a small negative bias (NMB = −11.1%). The linear regression shows a slope of 0.51 and intercept of 3.34 × 10^{15} molec. cm^{-2}, reflecting underestimation of POMINO-GEMS tropospheric NO_2 VCDs on high-NO_2 days.

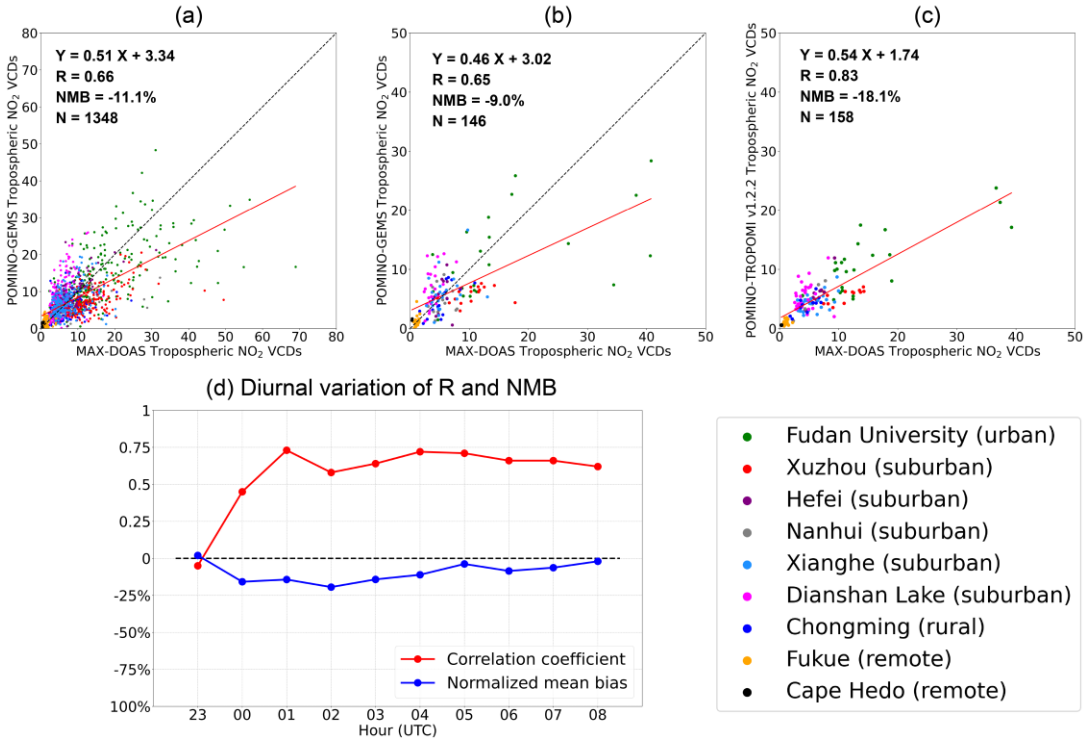

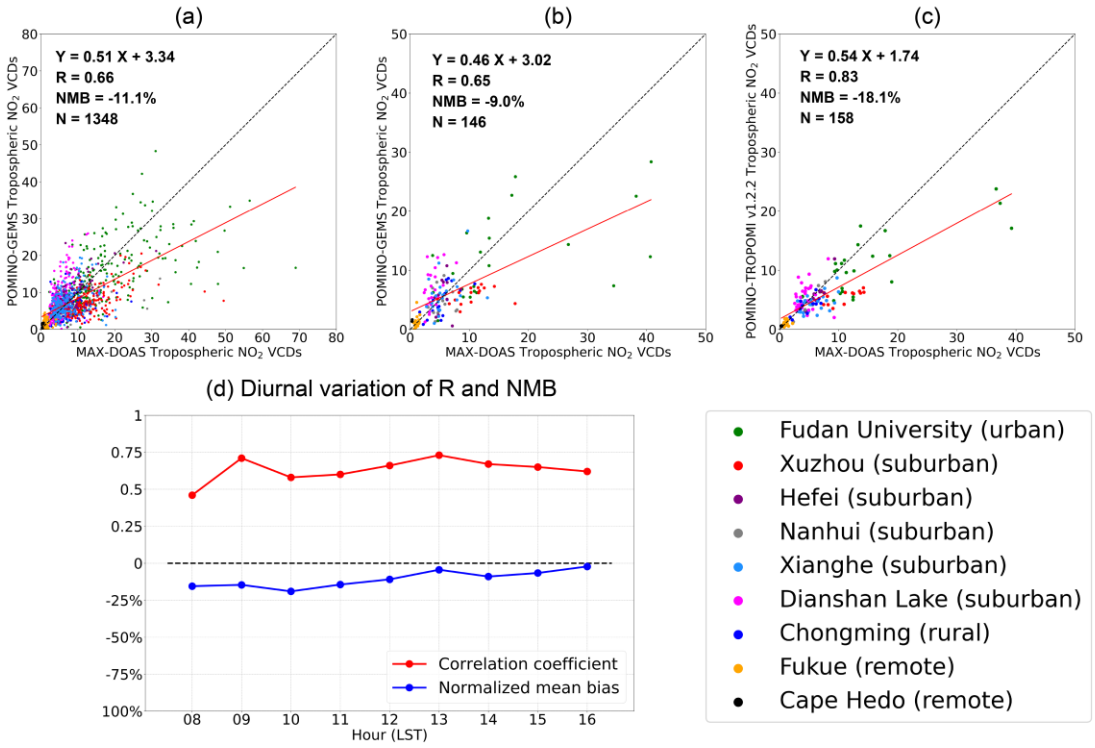

Figure 8. Evaluation of satellite NO_2 VCD data using ground-based MAX-DOAS measurements. (a) Scatterplot for tropospheric NO_2 VCDs ($\times 10^{15}$ molec. cm^{-2}) between MAX-DOAS and POMINO-GEMS at all GEMS observation hours in JJA 2021. Each data pair denotes an hour. (b-c) Scatterplots for tropospheric NO_2 VCDs ($\times 10^{15}$ molec. cm^{-2}) in JJA 2021 (b) between MAX-DOAS and POMINO-GEMS at 13:45 – 14:15 LST and (c) between MAX-DOAS and POMINO-TROPOMI v1.2.2. Each data pair denotes a day. Each MAX-DOAS station is color-coded. (d) Diurnal variations of spatiotemporal correlation coefficients and NMBs of POMINO-GEMS tropospheric NO_2 VCDs relative to ground-based MAX-DOAS data.

Figure 8b-c further use MAX-DOAS measurements to evaluate POMINO-GEMS and POMINO-TROPOMI v1.2.2 tropospheric NO_2 VCDs at the overpass time of TROPOMI. In Figure 8b, POMINO-GEMS data at 13:45 – 14:15 LST are used to match the overpass time of TROPOMI. The POMINO-TROPOMI product is evaluated in the context of understanding the relative performance of POMINO-GEMS. Each data point represents a day. Figure 8b-c show that the day-to-day variability of MAX-DOAS measurements is well captured by POMINO-TROPOMI v1.2.2 (R = 0.83), but less so by POMINO-GEMS (R = 0.65). Linear regression results show an underestimate of tropospheric NO_2 VCDs in POMINO-TROPOMI v1.2.2 (NMB = −18.1%), as also found in previous studies (Liu et al., 2020). POMINO-GEMS exhibits a small bias (NMB = −9.0%), but station-dependent performance is apparent. At the two remote sites of Fukue and Cape Hedo with low NO_2, POMINO-GEMS NO_2 columns are higher than those of MAX-DOAS measurements. At the other sites, the data pairs are more scattered and

located both above and below the 1:1 line, resulting in a small NMB.

Figure 8d shows the NMBs and correlation coefficients of POMINO-GEMS NO_2 VCDs relative to ground-based MAX-DOAS data at each hour. ~~The NMBs are negative at most hours except 23:00 UTC (07:00 BJT).~~ The negative NMBs reach a maximum of about 20% at ~~02:00 UTC (~~10:00 BJT~~),~~ and decrease to less than 10% in the afternoon. The correlation coefficients are modest or high (0.45 – 0.73) at ~~most hours, with the exception at the first hour which is likely due to few valid data (N = 17).~~all hours.

Figure 9 compares the diurnal variation of tropospheric NO_2 VCDs between POMINO-GEMS and MAX-DOAS at eight stations. At each site, NO_2 values are averaged in JJA 2021 at each hour for comparison, and the number of valid days for each hour is also shown. The Cape Hedo site is not included because there are few valid MAX-DOAS data points at each hour. Figure 10a-f show that at the urban and suburban sites, MAX-DOAS NO_2 (black lines) peaks in the mid-to-late morning, declines towards the minimum values at noon around 13:00 LST, and then gradually increases in the afternoon. Strong correlation of NO_2 diurnal variation between POMINO-GEMS (red solid lines) and MAX-DOAS is found at Xuzhou (R = 0.82), Hefei (R = 0.96), Fudan University (R = 0.84), Nanhui (R = 0.79) and Xianghe (R = 0.94). At the Dianshan Lake site, POMINO-GEMS NO_2 columns increase but MAX-DOAS data decrease from 08:00 to 09:00 LST, resulting in a lower correlation coefficient (R = 0.60). At Chongming and Fukue sites, MAX-DOAS NO_2 shows a peak in the morning without evident increase in the early afternoon, but this diurnal pattern is not fully captured by POMINO-GEMS. At Fukue, POMINO-GEMS NO_2 exhibit abrupt changes at 12:00 and 13:00 LST due to few valid data.

In addition, comparison of POMINO-GEMS diurnal variation with NO_2 data from GOME-2 in the morning and OMI and TROPOMI in the early afternoon shows good agreement at Hefei, Nanhui, Dianshan Lake, Chongming and Fukue sites. The differences between POMINO-GEMS to MAX-DOAS NO_2 VCDs are comparable or smaller than those between LEO satellite and MAX-DOAS NO_2 VCDs.

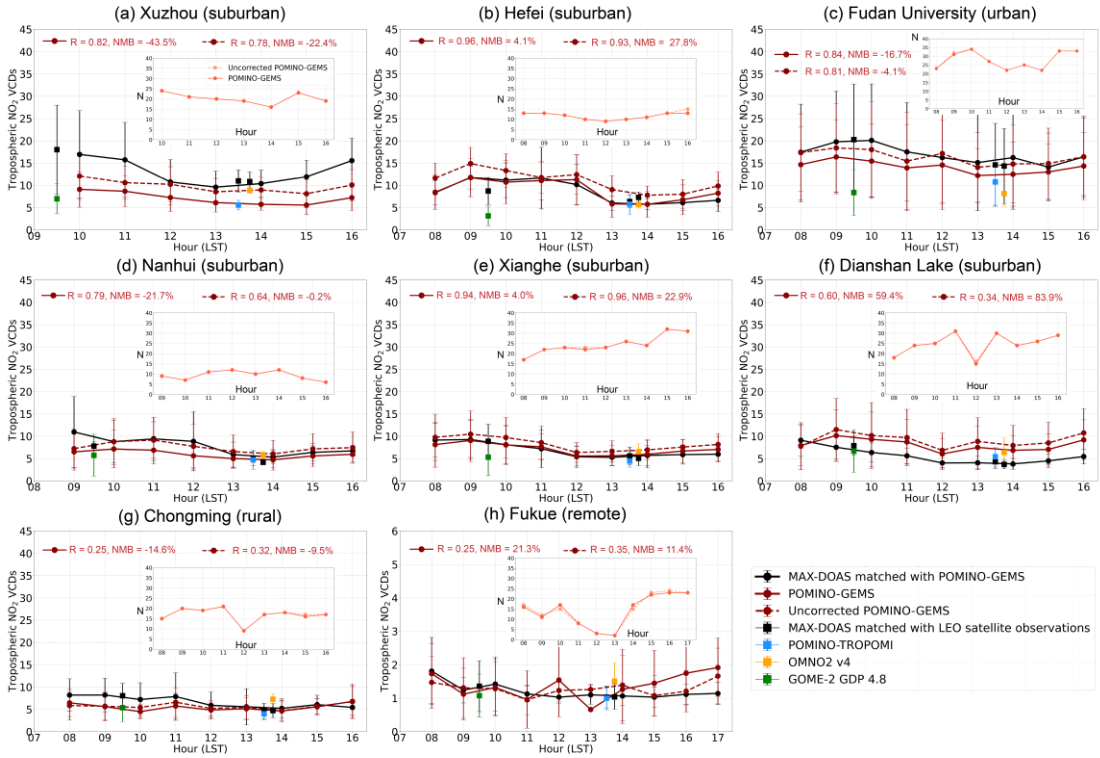

Figure 9. Diurnal variation of hourly tropospheric NO_2 VCDs ($\times 10^{15}$ molec. cm^{-2}) of MAX-DOAS (black lines), and POMINO-GEMS with TROPOMI correction (red solid lines). and re-calculated POMINO-GEMS without TROPOMI correction (red dashed lines) at eight sites in JJA 2021. The error bars denote the standard deviation of MAX-DOAS and POMINO-GEMS NO_2 at each hour, respectively. Diurnal correlation and all-hour-mean NMB of POMINO-GEMS against MAX-DOAS data are shown. The number of valid days for each hour is also presented. The black squares with an error bar represent the mean value and standard deviation of MAX-DOAS tropospheric NO_2 VCDs matched with POMINO-TROPOMI v1.2.2 (blue squares), OMNO2 v4 (orange squares) and GOME-2 GDP 4.8 (green squares), respectively.

As we use TROPOMI total NO_2 SCDs to correct those of GEMS, this may influence the NO_2 diurnal variation of original GEMS observations. Thus we also compare MAX-DOAS data with re-calculated POMINO-GEMS tropospheric NO_2 VCDs without correction in total SCDs (red dashed lines in Figure 9). Compared to our default POMINO-GEMS data (with correction), excluding the correction leads to lower diurnal correlation coefficients at Xuzhou, Hefei, Fudan University, Nanhui and Dianshan Lake, but higher correlation coefficients at Xianghe, Chongming and Fukue. Excluding the correction increases the NMB at three sites but decreases the NMB at five sites. We conclude that at these eight sites (in the eastern areas), no significant influence on the diurnal variation of POMINO-GEMS tropospheric NO_2 VCDs is brought in through TROPOMI-based correction for total NO_2 SCDs.

Figure 10 compares the diurnal variations between POMINO-GEMS and mobile-car MAX-DOAS tropospheric NO_2 VCD data in the Three Rivers' Source region on the Tibetan Plateau. Results of

POMINO-GEMS with and without total SCD correction are shown in the red solid and dashed lines, respectively. Mobile-car MAX-DOAS data show an evident decrease of tropospheric NO_2 VCDs from the morning to noon with little change thereafter. Such NO_2 diurnal patterns reflect the spatial and temporal variations of tropospheric NO_2 along the driving route. The high NO_2 values with large standard deviation at 09:00 BJT is due to enhanced pollution and variability in the morning when the car is in or near the Xining city. The NO_2 diurnal variations of POMINO-GEMS with correction correlate well with those of mobile-car MAX-DOAS data (R = 0.81). In contrast, POMINO-GEMS without total SCD correction exhibits much poorer correlation with mobile-car MAX-DOAS data, due to the erroneous increase in the afternoon.

Overall, the validation results with independent ground-based and mobile-car MAX-DOAS measurements provide confidence on the general characteristics of POMINO-GEMS NO_2 diurnal variations.

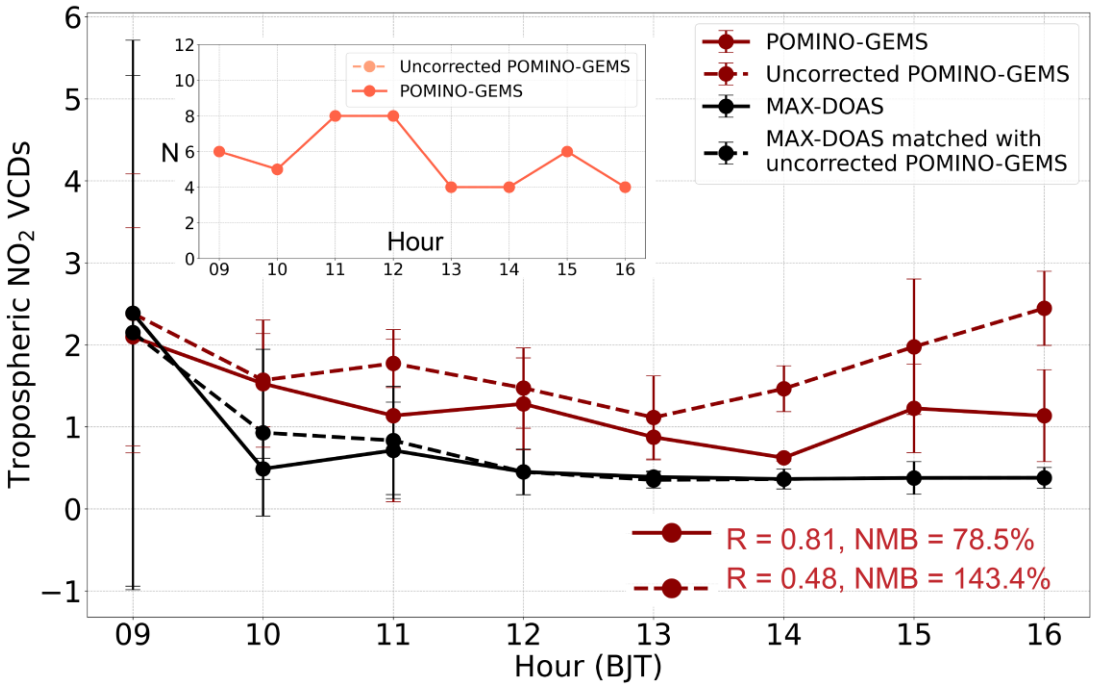

Figure 10. Diurnal variation of hourly mean tropospheric NO_2 VCDs (× 10^{15} molec. cm^{-2}) of mobile-car MAX-DOAS and POMINO-GEMS in the Three Rivers' Source region. The black solid lines denote MAX-DOAS data that spatiotemporally match with POMINO-GEMS with total SCD correction (red solid lines). The black dashed lines denote MAX-DOAS data that spatiotemporally match with POMINO-GEMS without correction (red dashed lines). The error bars denote the standard deviation of MAX-DOAS and POMINO-GEMS NO_2 at each hour during the field campaign, respectively. Values for diurnal correlation and mean NMB of POMINO-GEMS relative to MAX-DOAS are shown. The number of days with valid data for each hour is also presented.

3.4 Validation with surface NO_2 concentration measurements from MEE

The scatterplot in Figure 11a compares surface NO_2 concentrations derived from POMINO-GEMS with MEE measurements at all hours. POMINO-GEMS derived surface NO_2 concentrations show good agreement with MEE measurements in terms of spatiotemporal correlation (R = 0.78) and bias (NMB = −26.3%), but are higher than those of MEE at some high-value situations, which mainly occur over the YRD region (Figure S14). These differences reflect errors in POMINO-GEMS NO_2 VCDs, in the conversion from tropospheric VCDs to surface concentrations, and in MEE data (due to potential contamination by nitric acid and organic nitrates (Liu et al., 2018a)).

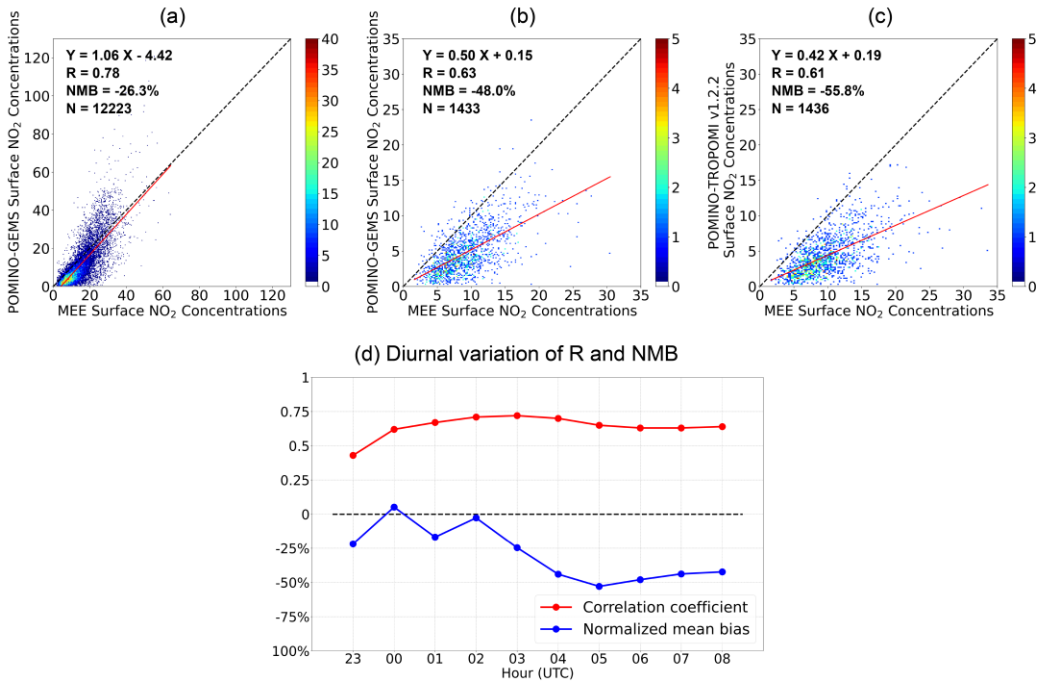

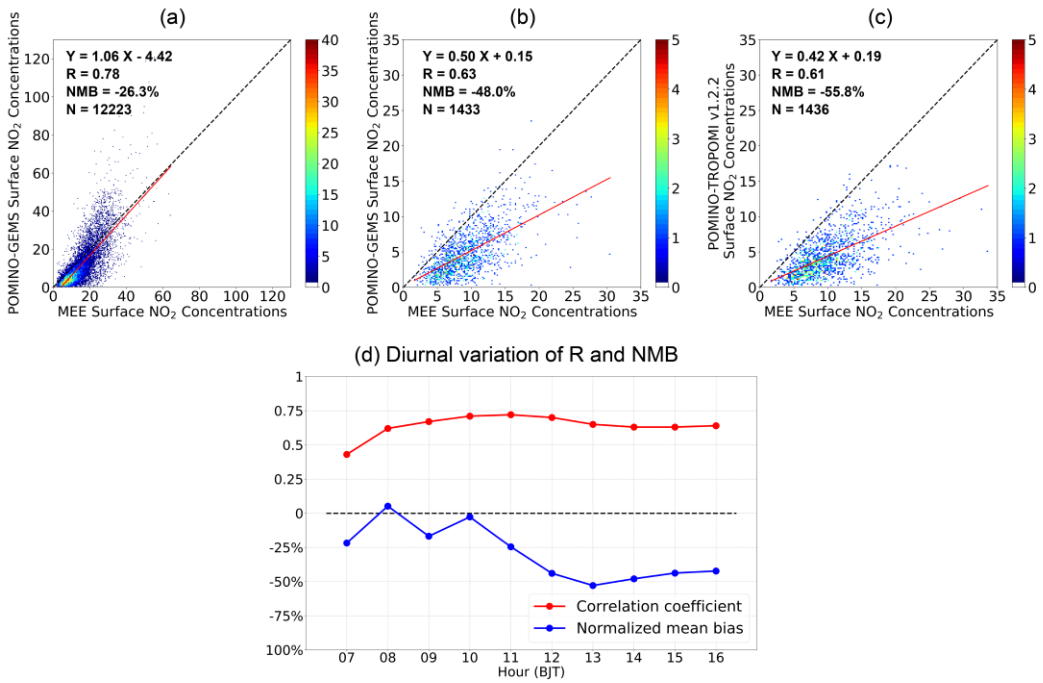

Figure 11. Evaluation of satellite-derived surface NO_2 concentrations (μg m^{-3}) using MEE measurements in JJA 2021. (a) Scatterplot for MEE and POMINO-GEMS at all GEMS observation hours averaged over all days in JJA 2021. (b) Scatterplot for MEE and POMINO-GEMS at 13:45 – 14:15 LST. (c) Scatterplot for MEE and POMINO-TROPOMI v1.2.2. The color bar represents the data density. (d) Diurnal variations of spatiotemporal correlation coefficients and NMBs of POMINO-GEMS derived surface NO_2 concentrations relative to MEE measurements.

Figure 11b-c show validation results for satellite-derived surface NO_2 concentrations with MEE measurements at the overpass time of TROPOMI (i.e., early afternoon). Here, each data pair denotes a MEE site. POMINO-GEMS results at 13:45 – 14:15 LST are used to match the overpass time of TROPOMI data. Overall, both satellite-based datasets show good spatial correlation with MEE measurements (R = 0.63 and 0.61). POMINO-GEMS exhibits higher linear regression slope (0.50) with smaller NMB (−48.0%). The values of satellite data are lower than those from MEE, especially in the afternoon (Figure 11d). This is in part because of the aforementioned contamination issues in MEE data, which becomes severer in the afternoon as the air gets more aged throughout the daytime.

Figure 12a examines the diurnal variation of surface NO_2 concentrations averaged over JJA 2021 at all sites. The MEE data show a smooth and monotonic decline from the early morning to the early afternoon, with a slight increase beginning at 15:00 LST. This diurnal pattern differs from those seen in ground-based MAX-DOAS VCD data (Figure 9), due to the difference in sampling size between MEE and MAX-DOAS, the diurnal variation of NO_2 vertical distribution that affects the relationship between surface and columnar NO_2, as well as the insensitivity of NO_2 columns to changes in PBL heights.

POMINO-GEMS derived surface NO_2 concentrations show similar diurnal variations to those of MEE (R = 0.97), although with a peak at 10:00 LST and a gradual increase beginning at 14:00 LST. The discrepancies between POMINO-GEMS and MEE surface NO_2 concentrations at different hours are likely caused by the assumed constant correction factor of 2 to account for the vertical gradient of NO_2 from the height of ground instrument to the center of the first model layer (Section 2.2). In the morning when the PBL is low, most NO_2 molecules are near the ground and the vertical gradient of NO_2 over polluted regions is the largest in the daytime, so the factor of 2 may lead to underestimation of derived surface NO_2 concentrations. In contrast, in the afternoon, the PBL mixing is much stronger and the vertical gradient of NO_2 is much smaller, thus the factor of 2 may lead to overestimated surface NO_2 concentrations. Note that the consistency between POMINO-GEMS and MEE data does not depend on the total SCD correction (Table S4).

To quantify the influences of the diurnal variation of hourly column-to-surface ratio from GEOS-Chem simulations, we compare the MEE measurements with POMINO-GEMS derived surface NO_2 concentrations using daily column-to-surface ratio (Figure S15). As expected, POMINO-GEMS derived NO_2 concentrations show a similar diurnal variation as the tropospheric NO_2 VCDs do, with two peaks in the mid-morning and afternoon, and a minimum at noon. The temporal correlation coefficient with MEE is only about 0.23. Thus it is more reasonable to use hourly ratio for comparison with MEE measurements, as done in our study.

To further test the reliability of our VCD-to-surface-concentration conversion method (Eq. (9)), we apply the same method to MAX-DOAS NO_2 VCDs and compare the resulting surface NO_2 concentrations with MEE data. As shown in Figure S16, the diurnal variation of MAX-DOAS derived surface NO_2 concentrations correlates well with that of MEE measurements (R = 0.96), in support of our conversion method.

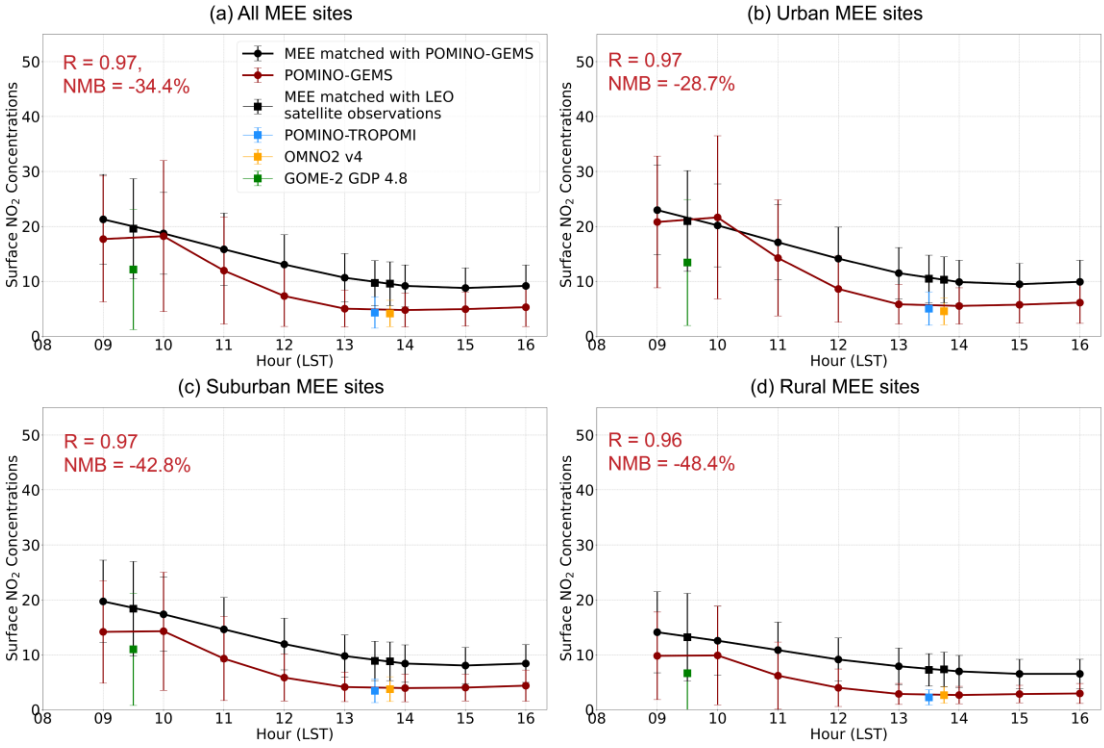

Figure 12. Diurnal variation of hourly surface NO_2 concentrations (μg m^{-3}) of MEE (back lines) and POMINO-GEMS (red lines) in JJA 2021. (a) At all MEE sites, (b) at urban sites, (c) at suburban sites and (d) at rural sites. The error bars denote the standard deviation of MEE and POMINO-GEMS derived surface NO_2 concentrations at each hour in JJA 2021, respectively. Diurnal correlation and mean NMB of POMINO-GEMS relative to MEE are also listed. The black squares with an error bar represent the mean value and standard deviation of MEE data matched with POMINO-TROPOMI v1.2.2 (blue squares), OMNO2 v4 (orange squares) and GOME-2 GDP 4.8 (green squares), respectively.

Figure 12b-d show the comparison of NO_2 diurnal variations for different groups of MEE sites. The diurnal variations of POMINO-GEMS derived surface NO_2 concentrations show similar characteristics over urban, suburban and rural regions, and all correlate well with those of MEE data. Meanwhile, surface NO_2 concentrations derived from LEO satellite observations also agree well with those of POMINO-GEMS, except that POMINO-GEMS derived surface NO_2 concentrations are higher than those of GOME-2 GDP 4.8 by about 40% – 60%. We conclude that validation with extensive MEE measurements presents promising performance of POMINO-GEMS retrievals, especially the great agreement of POMINO-GEMS NO_2 diurnal variation with MEE data over urban, suburban and rural regions.

3.5 Error estimates for POMINO-GEMS tropospheric NO_2 VCDs

Total retrieval errors for POMINO-GEMS tropospheric NO_2 VCDs are derived from the calculations of total SCDs, stratospheric SCDs, and tropospheric AMFs. Spatial and temporal averaging

675 across GEMS pixels can greatly reduce the random errors, but will not affect the systematic errors. Here,
676 we provide a preliminary estimate of POMINO-GEMS errors for the summertime retrieval discussed
677 above.

678 As described in Section 2, we calculate hourly total SCDs based on the original GEMS SCD data
679 and daily TROPOMI-guided corrections. According to the GEMS ATBD of NO_2 retrieval algorithm, the
680 SCD errors from the DOAS method are < 5.65% at high-NO_2 conditions (NO_2 VCD > 1×10^{15} molec.
681 cm^{-2}) (Lee et al., 2020). The NO_2 SCD errors of TROPOMI are reported to be $0.5 – 0.6 \times 10^{15}$ molec.
682 cm^{-2} (10% in a relative sense) (Van Geffen et al., 2022a). Given the assumption we made in adjusting
683 GEMS total SCDs to match TROPOMI values, we tentatively estimate the error in our corrected total
684 SCD data to be $0.5 – 0.7 \times 10^{15}$ molec. cm^{-2} (10% in a relative sense) for most regions and 0.9×10^{15}
685 molec. cm^{-2} (20% – 30%) at the edge of the northwestern GEMS FOV.

686 In constructing the stratospheric NO_2 SCDs, the stratospheric VCDs are taken from TROPOMI PAL
687 v2.3.1, scaled based on GEOS-CF v1 stratospheric NO_2 to account for diurnal variation, and then applied
688 with geometric AMFs. We assign a constant error of 0.2×10^{15} molec. cm^{-2} (5% – 10%) to our hourly
689 stratospheric SCDs, the same as the value for TROPOMI (Van Geffen et al., 2022a). Few studies have
690 assessed the accuracy of stratospheric NO_2 and its diurnal variation from GEOS-CF data (Knowland et
691 al., 2022b), but our comparison between GEOS-CF and TROPOMI shows great consistency (Section
692 2.1.5). As most of the errors in total SCDs are absorbed in the stratosphere-troposphere separation step
693 (Van Geffen et al., 2015), the errors in tropospheric SCDs should be 10% – 30% depending on different
694 cases, with higher relative biases in cleaner situations.

695 Tropospheric AMF calculations are the dominant error source for retrieved tropospheric NO_2 VCDs
696 over polluted regions. According to Liu et al. (2020), the AMF errors caused by uncertainty in surface
697 reflectance are about 10%, and errors induced by uncertainties in aerosol parameters are about 10% in
698 clean regions and 20% for heavily polluted situations. We further assume that the O_2-O_2 cloud retrieval
699 algorithm introduces another error at the 10% level to the NO_2 AMFs. The uncertainty in a priori NO_2
700 vertical profiles is estimated to cause an AMF error by 10% (Liu et al., 2020). Yang et al. (2023)
701 suggested that the NO_2 profiles from GEOS-Chem (version 13.3.4) might contain incorrect timing of
702 PBL mixing growth in the morning and thus introduce a relative root-mean-square error of 7.6% and
703 NMB of 2.7% in AMF; however, this error could be greatly dampened by averaging over a long time

period. The free tropospheric NO_2 bias in GEOS-Chem NO_2 profiles might also contribute to the retrieval errors especially over remote regions. Adding these errors in quadrature leads to the overall AMF errors for POMINO-GEMS at 20% – 40%.

The overall uncertainty in POMINO-GEMS tropospheric NO_2 VCDs is estimated by adding in quadrature the errors in tropospheric NO_2 SCDs and AMFs, when these errors are expressed in the relative sense. For remote regions with low tropospheric NO_2 abundances, the overall retrieval uncertainties can reach 30% – 50% and are dominated by errors in tropospheric SCDs. For regions with abundant tropospheric NO_2, the uncertainties of retrieved tropospheric VCDs are dominated by the AMF errors and are estimated to be about 20% – 30%.

As shown in Figure 8d and Figure 11d, the maximum negative NMB of POMINO-GEMS tropospheric NO_2 VCDs relative to ground-based MAX-DOAS data is about 20% in the mid-morning, and the NMB of POMINO-GEMS derived surface NO_2 concentrations to MEE measurements is −30% on average. Thus our estimated error magnitude is supported by the independent ground-based MAX-DOAS and MEE data.

4. Conclusions

The GEMS instrument provides an unprecedented opportunity for air quality monitoring at a high spatiotemporal resolution. Our POMINO-GEMS algorithm retrieves tropospheric NO_2 VCDs as a research product. The algorithm first calculates hourly tropospheric NO_2 SCDs through fusion of total NO_2 SCDs from the GEMS v1.0 L2 NO_2 product, total and stratospheric NO_2 columns from the TROPOMI PAL v2.3.1 L2 NO_2 product, and stratospheric NO_2 diurnal variations from the GEOS-CF v1 dataset. The fusion approach reduces the high bias in total SCDs and removes the stripe-like patterns in the official GEMS v1.0 product. Our algorithm then calculates tropospheric NO_2 AMFs to convert SCDs to VCDs. A preliminary estimate of retrieval errors is also given.

Our initial POMINO-GEMS data for JJA 2021 shows high values of tropospheric NO_2 VCDs with clear hotspots ($> 10 \times 10^{15}$ molec. cm^{-2}) over regions where anthropogenic emissions of NO_x are abundant. The spatial gradients of tropospheric NO_2 VCDs from urban centers to surrounding areas are substantial in the morning due to traffic emissions, but the gradients are much reduced at noon and in the afternoon. A gradual increase of tropospheric NO_2 VCDs from the morning to noon is observed over clean regions of western China, likely as a result of enhanced biogenic emissions. Over high NO_2 regions where

anthropogenic activities dominate the NO_x emissions, NO_2 columns increase until a peak at 09:00 – 10:00 LST, decrease to the minimum at noon and then increase in the afternoon again. Such characteristics of NO_2 diurnal variations are associated with the changes in natural and anthropogenic NO_x emissions, photochemistry and atmospheric transport.

POMINO-GEMS tropospheric NO_2 VCDs agree well with POMINO-TROPOMI v1.2.2 in terms of spatial correlation (0.98) and NMB (4.9%). POMINO-GEMS data are also consistent with the OMNO2 v4 tropospheric NO_2 VCD product in the early afternoon and GOME-2 GDP 4.8 tropospheric NO_2 VCD product in the morning, with R of 0.87 and 0.83, and NMB of −16.8% and −1.5%, respectively.

POMINO-GEMS tropospheric NO_2 VCDs are comparable with ground-based MAX-DOAS measurements at nine ground-based sites with a small NMB (−11.1%), although the correlation is modest (R = 0.66). Both the bias and correlation values are smaller than POMINO-TROPOMI v1.2.2 (NMB = −18.1%, R = 0.83). More importantly, POMINO-GEMS well captures the diurnal variation of MAX-DOAS NO_2 VCDs at Xuzhou (R = 0.82), Hefei (R = 0.96), Fudan University (R = 0.84), Nanhui (R = 0.79), Xianghe (R = 0.94) and Dianshan Lake (R = 0.60) sites, although the correlations are relatively poor at Chongming and Fukue sites. Comparison with mobile-car MAX-DOAS measurements in the Three Rivers' Source region on the Tibetan Plateau also shows good correlation in NO_2 diurnal variation (R = 0.81).

We also compare surface NO_2 concentrations derived from tropospheric NO_2 VCDs in POMINO-GEMS and POMINO-TROPOMI v1.2.2 against MEE data, taking advantage of the large number of MEE sites. POMINO-GEMS derived surface NO_2 concentration data exhibit a small NMB (–26.3%). For these sites at TROPOMI overpass times, POMINO-GEMS derived surface NO_2 concentrations show a smaller magnitude of NMB (−48.0%) than POMINO-TROPOMI v1.2.2 (−55.8%). Excellent agreement in diurnal variation between POMINO-GEMS derived and MEE NO_2 is exhibited over all (R = 0.97), urban (R = 0.97), suburban (R = 0.97) and rural (R = 0.96) sites.

Overall, our comprehensive validation process highlights the good performance of POMINO-GEMS tropospheric NO_2 VCD product, both in magnitude and spatiotemporal variation. However, there are still several limitations in our study. To address the systematic overestimation and stripes problems in the original GEMS data, we correct GEMS total NO_2 SCDs by using TROPOMI data as a temporary solution. For example, we implement a simple geometric correction to combine GEMS and TROPOMI

762 total NO_2 SCDs, but their differences in scattering geometry are only partly accounted for. Thus this
763 correction works well in most regions, but may introduce SCD uncertainties up to 0.9×10^{15} molec. cm^{-2}
764 (20% – 30%) at the edge of the northwestern GEMS FOV. Currently, the Environmental Satellite Center
765 of South Korea is updating the NO_2 SCD data to v2.0. We will update our POMINO-GEMS algorithm
766 accordingly, once the updated official NO_2 product becomes available to provide necessary inputs for
767 our research product. In addition, in the conversion from NO_2 VCDs to surface concentrations, we use a
768 constant correction factor of 2 to account for the strong NO_2 vertical gradient near the surface. This
769 simple treatment does not account for the diurnal variation of the correction factor, and thus may
770 introduce errors in the derived surface NO_2 concentrations. Nevertheless, the current POMINO-GEMS
771 data serve as our initial attempt to derive the diurnal variations of tropospheric NO_2 at a high
772 spatiotemporal resolution from GEMS, and they are expected to offer a useful source of information for
773 various applications such as air quality analysis and emission constraint.
774
775 *Data availability*. The POMINO-GEMS NO_2 data will be freely available soon at the ACM group
776 product website (http://www.pku-atmos-acm.org/acmProduct.php/). The TROPOMI PAL v2.3.1 L2
777 product can be downloaded from https://data-portal.s5p-pal.com. The OMNO2 v4 L2 product can be
778 downloaded from https://aura.gesdisc.eosdis.nasa.gov/data/Aura_OMI_Level2/OMNO2.003/. The
779 GOME-2 GDP 4.8 L2 product can be downloaded from http://acsaf.org/ after registration. The GEOS-
780 CF v1.0 dataset can be downloaded from https://gmao.gsfc.nasa.gov/weather_prediction/GEOS-
781 CF/data_access/. The MEE surface NO_2 measurements can be downloaded from https://quotsoft.net/air/.
782 The ground-based and mobile-car MAX-DOAS measurements can be provided upon requests to the
783 corresponding owners.
784
785 *Author contributions*. JL conceived this research. YZ and JL designed the algorithm and validation
786 process. YZ performed all calculations with additional code support from HK. YZ and JL wrote the paper.
787 RS provided LIDORT. JK, HL, JP and HH provided GEMS data. MVR, FH, TiW, PW, QH, KQ, YC,
788 YK, JX, PX, XT, SZ and SW provided the ground-based MAX-DOAS measurements. SC, XC, JM and
789 ThW provided the mobile-car MAX-DOAS measurements. HK helped process MEE measurements. LC
790 and ML helped analyze the validation results. All authors commented on the paper.

Competing interests. The authors declare that they have no conflicts of interest.

Financial support. This research has been supported by the National Natural Science Foundation of China (grant no. 42075175) and the Second Tibetan Plateau Scientific Expedition and Research Program (grant no. 2019QZKK0604).

References

Beirle, S., Boersma, K. F., Platt, U., Lawrence, M. G., and Wagner, T.: Megacity Emissions and Lifetimes of Nitrogen Oxides Probed from Space, Science, 333, 1737-1739, 10.1126/science.1207824, 2011.

Biswas, M. S. and Mahajan, A. S.: Year-long Concurrent MAX-DOAS Observations of Nitrogen Dioxide and Formaldehyde at Pune: Understanding Diurnal and Seasonal Variation Drivers, Aerosol and Air Quality Research, 21, 200524, 10.4209/aaqr.200524, 2021.

Boersma, K. F., Eskes, H. J., and Brinksma, E. J.: Error analysis for tropospheric NO2retrieval from space, Journal of Geophysical Research: Atmospheres, 109, n/a-n/a, 10.1029/2003jd003962, 2004.

Boersma, K. F., Jacob, D. J., Eskes, H. J., Pinder, R. W., Wang, J., and Van Der A, R. J.: Intercomparison of SCIAMACHY and OMI tropospheric NO₂columns: Observing the diurnal evolution of chemistry and emissions from space, Journal of Geophysical Research, 113, 10.1029/2007jd008816, 2008.

Boersma, K. F., Jacob, D. J., Trainic, M., Rudich, Y., Desmedt, I., Dirksen, R., and Eskes, H. J.: Validation of urban NO₂ concentrations and their diurnal and seasonal variations observed from the SCIAMACHY and OMI sensors using in situ surface measurements in Israeli cities, Atmospheric Chemistry and Physics, 9, 3867-3879, 10.5194/acp-9-3867-2009, 2009.

Boersma, K. F., Eskes, H. J., Dirksen, R. J., van der A, R. J., Veefkind, J. P., Stammes, P., Huijnen, V., Kleipool, Q. L., Sneep, M., Claas, J., Leitão, J., Richter, A., Zhou, Y., and Brunner, D.: An improved tropospheric NO2 column retrieval algorithm for the Ozone Monitoring Instrument, Atmospheric Measurement Techniques, 4, 1905-1928, 10.5194/amt-4-1905-2011, 2011.

Burrows, J. P.: The Global Ozone Monitoring Experiment (GOME) : Mission concept and first

820 scientific results, Journal of Atmospheric Sciences, 56, 2340-2352, 1999.
821 Callies, J., Corpaccioli, E., Eisinger, M., Hahne, A., and Lefebvre, A.: GOME-2 – Metop ' s Second-
822 Generation Sensor for Operational Ozone Monitoring,
823 Chen, L., Lin, J., Martin, R., Du, M., Weng, H., Kong, H., Ni, R., Meng, J., Zhang, Y., Zhang, L.,
824 and van Donkelaar, A.: Inequality in historical transboundary anthropogenic PM2.5 health impacts,
825 Science Bulletin, https://doi.org/10.1016/j.scib.2021.11.007, 2021.
826 Chen, L., Lin, J., Ni, R., Kong, H., Du, M., Yan, Y., Liu, M., Wang, J., Weng, H., Zhao, Y., Li, C.,
827 and Martin, R. V.: Historical transboundary ozone health impact linked to affluence, Environmental
828 Research Letters, 17, 104014, 10.1088/1748-9326/ac9009, 2022.
829 Cheng, S., Cheng, X., Ma, J., Xu, X., Zhang, W., Lv, J., Bai, G., Chen, B., Ma, S., Ziegler, S.,
830 Donner, S., and Wagner, T.: Mobile MAX-DOAS observations of tropospheric NO2 and HCHO during
831 summer over the Three Rivers' Source region in China, Atmos. Chem. Phys., 23, 3655-3677,
832 10.5194/acp-23-3655-2023, 2023.
833 Cooper, M. J., Martin, R. V., Hammer, M. S., Levelt, P. F., Veefkind, P., Lamsal, L. N., Krotkov, N.
834 A., Brook, J. R., and Mclinden, C. A.: Global fine-scale changes in ambient NO2 during COVID-19
835 lockdowns, Nature, 601, 380-387, 10.1038/s41586-021-04229-0, 2022.
836 Crutzen, P. J.: The influence of nitrogen oxides on the atmospheric ozone content, Quarterly Journal
837 of the Royal Meteorological Society, 96, 320-325, 10.1002/qj.49709640815, 1970.
838 Cui, Y., Lin, J., Song, C., Liu, M., Yan, Y., Xu, Y., and Huang, B.: Rapid growth in nitrogen dioxide
839 pollution over Western China, 2005–2013, Atmos. Chem. Phys., 16, 6207-6221, 10.5194/acp-16-6207-
840 2016, 2016.
841 Dirksen, R. J., Boersma, K. F., Eskes, H. J., Ionov, D. V., Bucsela, E. J., Levelt, P. F., and Kelder, H.
842 M.: Evaluation of stratospheric NO2retrieved from the Ozone Monitoring Instrument: Intercomparison,
843 diurnal cycle, and trending, Journal of Geophysical Research, 116, 10.1029/2010jd014943, 2011.
844 Eastham, S. D., Weisenstein, D. K., and Barrett, S. R. H.: Development and evaluation of the unified
845 tropospheric–stratospheric chemistry extension (UCX) for the global chemistry-transport model GEOS-
846 Chem, Atmospheric Environment, 89, 52-63, https://doi.org/10.1016/j.atmosenv.2014.02.001, 2014.
847 Eskes, H., Van Geffen, J., Sneep, M., Veefkind, P., Niemeier, S., and Zehner, C.: S5P Nitrogen
848 Dioxide v02.03.01 intermediate reproecessing on the S5P-PAL system: Readme file, 2021.

Ghude, S. D., Karumuri, R. K., Jena, C., Kulkarni, R., Pfister, G. G., Sajjan, V. S., Pithani, P., Debnath, S., Kumar, R., Upendra, B., Kulkarni, S. H., Lal, D. M., Vander A, R. J., and Mahajan, A. S.: What is driving the diurnal variation in tropospheric NO2 columns over a cluster of high emission thermal power plants in India?, Atmospheric Environment: X, 5, 100058, https://doi.org/10.1016/j.aeaoa.2019.100058, 2020.

Grubbs, F. E.: Sample Criteria for Testing Outlying Observations, The Annals of Mathematical Statistics, 21, 27-58, 10.1214/aoms/1177729885, 1950.

Gu, D., Wang, Y., Smeltzer, C., and Boersma, K. F.: Anthropogenic emissions of NOxover China: Reconciling the difference of inverse modeling results using GOME-2 and OMI measurements, Journal of Geophysical Research: Atmospheres, 119, 7732-7740, 10.1002/2014jd021644, 2014.

Hendrick, F., Müller, J.-F., Clémer, K., Wang, P., De Mazière, M., Fayt, C., Gielen, C., Hermans, C., Ma, J. Z., Pinardi, G., Stavrakou, T., Vlemmix, T., and Van Roozendael, M.: Four years of ground-based MAX-DOAS observations of HONO and NO₂ in the Beijing area, Atmospheric Chemistry and Physics, 14, 765-781, 10.5194/acp-14-765-2014, 2014.

Herman, J., Abuhassan, N., Kim, J., Kim, J., Dubey, M., Raponi, M., and Tzortziou, M.: Underestimation of column NO2 amounts from the OMI satellite compared to diurnally varying ground-based retrievals from multiple PANDORA spectrometer instruments, Atmos. Meas. Tech., 12, 5593-5612, 10.5194/amt-12-5593-2019, 2019.

Hoek, G., Krishnan, R. M., Beelen, R., Peters, A., Ostro, B., Brunekreef, B., and Kaufman, J. D.: Long-term air pollution exposure and cardio- respiratory mortality: a review, Environmental Health, 12, 43, 10.1186/1476-069X-12-43, 2013.

Jing, B., Wu, L., Mao, H., Gong, S., He, J., Zou, C., Song, G., Li, X., and Wu, Z.: Development of a vehicle emission inventory with high temporal–spatial resolution based on NRT traffic data and its impact on air pollution in Beijing – Part 1: Development and evaluation of vehicle emission inventory, Atmospheric Chemistry and Physics, 16, 3161-3170, 10.5194/acp-16-3161-2016, 2016.

Kanaya, Y., Irie, H., Takashima, H., Iwabuchi, H., Akimoto, H., Sudo, K., Gu, M., Chong, J., Kim, Y. J., Lee, H., Li, A., Si, F., Xu, J., Xie, P.-H., Liu, W.-Q., Dzhola, A., Postylyakov, O., Ivanov, V., Grechko, E., Terpugova, S., and Panchenko, M.: Long-term MAX-DOAS network observations of NO₂ in Russia and Asia (MADRAS) during the period 2007–2012: instrumentation,

878 elucidation of climatology, and comparisons with OMI satellite observations and global model si,
879 Atmospheric Chemistry and Physics, 14, 7909-7927, 10.5194/acp-14-7909-2014, 2014.
880 Keller, C. A., Knowland, K. E., Duncan, B. N., Liu, J., Anderson, D. C., Das, S., Lucchesi, R. A.,
881 Lundgren, E. W., Nicely, J. M., Nielsen, E., Ott, L. E., Saunders, E., Strode, S. A., Wales, P. A., Jacob, D.
882 J., and Pawson, S.: Description of the NASA GEOS Composition Forecast Modeling System GEOS-CF
883 v1.0, Journal of Advances in Modeling Earth Systems, 13, 10.1029/2020ms002413, 2021.
884 Kim, J., Jeong, U., Ahn, M.-H., Kim, J. H., Park, R. J., Lee, H., Song, C. H., Choi, Y.-S., Lee, K.-
885 H., Yoo, J.-M., Jeong, M.-J., Park, S. K., Lee, K.-M., Song, C.-K., Kim, S.-W., Kim, Y. J., Kim, S.-W.,
886 Kim, M., Go, S., Liu, X., Chance, K., Chan Miller, C., Al-Saadi, J., Veihelmann, B., Bhartia, P. K., Torres,
887 O., Abad, G. G., Haffner, D. P., Ko, D. H., Lee, S. H., Woo, J.-H., Chong, H., Park, S. S., Nicks, D., Choi,
888 W. J., Moon, K.-J., Cho, A., Yoon, J., Kim, S.-K., Hong, H., Lee, K., Lee, H., Lee, S., Choi, M., Veefkind,
889 P., Levelt, P. F., Edwards, D. P., Kang, M., Eo, M., Bak, J., Baek, K., Kwon, H.-A., Yang, J., Park, J.,
890 Han, K. M., Kim, B.-R., Shin, H.-W., Choi, H., Lee, E., Chong, J., Cha, Y., Koo, J.-H., Irie, H., Hayashida,
891 S., Kasai, Y., Kanaya, Y., Liu, C., Lin, J., Crawford, J. H., Carmichael, G. R., Newchurch, M. J., Lefer,
892 B. L., Herman, J. R., Swap, R. J., Lau, A. K. H., Kurosu, T. P., Jaross, G., Ahlers, B., Dobber, M., Mcelroy,
893 C. T., and Choi, Y.: New Era of Air Quality Monitoring from Space: Geostationary Environment
894 Monitoring Spectrometer (GEMS), Bulletin of the American Meteorological Society, 101, E1-E22,
895 10.1175/bams-d-18-0013.1, 2020.
896 Kim, S., Kim, D., Hong, H., Chang, L. S., Lee, H., Kim, D. R., Kim, D., Yu, J. A., Lee, D., Jeong,
897 U., Song, C. K., Kim, S. W., Park, S. S., Kim, J., Hanisco, T. F., Park, J., Choi, W., and Lee, K.: First-
898 time comparison between NO2 vertical columns from GEMS and Pandora measurements, Atmos. Meas.
899 Tech. Discuss., 2023, 1-22, 10.5194/amt-2023-11, 2023.
900 Knowland, K. E., Keller, C. A., and Lucchesi, R. A.: File Specification for GEOS-CF Products,
901 2022a.
902 Knowland, K. E., Keller, C. A., Wales, P. A., Wargan, K., Coy, L., Johnson, M. S., Liu, J., Lucchesi,
903 R. A., Eastham, S. D., Fleming, E., Liang, Q., Leblanc, T., Livesey, N. J., Walker, K. A., Ott, L. E., and
904 Pawson, S.: NASA GEOS Composition Forecast Modeling System GEOS-CF v1.0: Stratospheric
905 Composition, Journal of Advances in Modeling Earth Systems, 14, e2021MS002852,
906 https://doi.org/10.1029/2021MS002852, 2022b.

Kong, H., Lin, J., Chen, L., Zhang, Y., Yan, Y., Liu, M., Ni, R., Liu, Z., and Weng, H.: Considerable Unaccounted Local Sources of NOx Emissions in China Revealed from Satellite, Environmental Science & Technology, 56, 7131-7142, 10.1021/acs.est.1c07723, 2022a.

Kong, H., Lin, J., Zhang, Y., Li, C., Xu, C., Shen, L., Liu, X., Yang, K., Su, H., and Xu, W.: Unexpected high NOX emissions from lakes on Tibetan Plateau under rapid warming, 10.21203/rs.3.rs-1980236/v1, 2022b.

Kong, H., Lin, J., Zhang, Y., Li, C., Xu, C., Shen, L., Liu, X., Yang, K., Su, H., and Xu, W.: High natural nitric oxide emissions from lakes on Tibetan Plateau under rapid warming, Nature Geoscience, 16, 474-477, 10.1038/s41561-023-01200-8, 2023.

Krotkov, N~~., Lamsal, L. N., Marchenko, S., and Swartz, W. H.: OMNO2 README Document Data Product Version 4.0, 2019~~. A., McLinden, C. A., Li, C., Lamsal, L. N., Celarier, E. A., Marchenko, S. V., Swartz, W. H., Bucsela, E. J., Joiner, J., Duncan, B. N., Boersma, K. F., Veefkind, J. P., Levelt, P. F., Fioletov, V. E., Dickerson, R. R., He, H., Lu, Z., and Streets, D. G.: Aura OMI observations of regional SO2 and NO2 pollution changes from 2005 to 2015, Atmos. Chem. Phys., 16, 4605-4629, 10.5194/acp-16-4605-2016, 2016.

Lamsal, L. N., Krotkov, N. A., ~~McLinden, C.~~Vasilkov, A., ~~Li, C., Lamsal, L. N., Celarier, E. A.,~~ Marchenko, S~~. V.~~, Qin, W., Yang, E.-S., Fasnacht, Z., Joiner, J., Choi, S., Haffner, D., Swartz, W. H., Fisher, B., and Bucsela, E~~. J., Joiner, J., Duncan, B. N., Boersma, K. F., Veefkind, J. P., Levelt, P. F., Fioletov, V. E., Dickerson, R. R., He, H., Lu, Z., and Streets, D. G.~~:.: Ozone Monitoring Instrument (OMI) Aura ~~OMI observations of regional SO2~~nitrogen dioxide standard product version 4.0 with improved surface and ~~NO2 pollution changes from 2005 to 2015, Atmos. Chem. Phys., 16, 4605-4629~~cloud treatments, Atmospheric Measurement Techniques, 14, 455-479, 10.5194/~~acp-16-4605-2016, 2016~~amt-14-455-2021, 2021.

Lee, H., Park, J., and Hong, H.: Geostationary Environment Monitoring Spectrometer (GEMS) Algorithm Theoretical Basis Document NO2 Retrieval Algorithm, 2020.

Lee, Y., Ahn, M. H., Kang, M., and Eo, M.: Spectral replacement using machine learning methods for continuous mapping of the Geostationary Environment Monitoring Spectrometer (GEMS), Atmos. Meas. Tech., 16, 153-168, 10.5194/amt-16-153-2023, 2023.

Levelt, P. F., Van Den Oord, G. H. J., Dobber, M. R., Malkki, A., Visser, H., Vries, J. D., Stammes,

P., Lundell, J. O. V., and Saari, H.: The ozone monitoring instrument, IEEE Transactions on Geoscience and Remote Sensing, 44, 1093-1101, 10.1109/tgrs.2006.872333, 2006.

Li, J., Wang, Y., Zhang, R., Smeltzer, C., Weinheimer, A., Herman, J., Boersma, K. F., Celarier, E. A., Long, R. W., Szykman, J. J., Delgado, R., Thompson, A. M., Knepp, T. N., Lamsal, L. N., Janz, S. J., Kowalewski, M. G., Liu, X., and Nowlan, C. R.: Comprehensive evaluations of diurnal NO2 measurements during DISCOVER-AQ 2011: effects of resolution-dependent representation of NOx emissions, Atmos. Chem. Phys., 21, 11133-11160, 10.5194/acp-21-11133-2021, 2021a.

Li, K.-F., Khoury, R., Pongetti, T. J., Sander, S. P., Mills, F. P., and Yung, Y. L.: Diurnal variability of stratospheric column NO₂ measured using direct solar and lunar spectra over Table Mountain, California (34.38° N), Atmospheric Measurement Techniques, 14, 7495-7510, 10.5194/amt-14-7495-2021, 2021b.

Lin, J. T. and McElroy, M. B.: Detection from space of a reduction in anthropogenic emissions of nitrogen oxides during the Chinese economic downturn, Atmos. Chem. Phys., 11, 8171-8188, 10.5194/acp-11-8171-2011, 2011.

Lin, J. T., Liu, M. Y., Xin, J. Y., Boersma, K. F., Spurr, R., Martin, R., and Zhang, Q.: Influence of aerosols and surface reflectance on satellite NO2 retrieval: seasonal and spatial characteristics and implications for NOx emission constraints, Atmospheric Chemistry and Physics, 15, 11217-11241, 10.5194/acp-15-11217-2015, 2015.

Lin, J. T., Martin, R. V., Boersma, K. F., Sneep, M., Stammes, P., Spurr, R., Wang, P., Van Roozendael, M., Clémer, K., and Irie, H.: Retrieving tropospheric nitrogen dioxide from the Ozone Monitoring Instrument: effects of aerosols, surface reflectance anisotropy, and vertical profile of nitrogen dioxide, Atmospheric Chemistry and Physics, 14, 1441-1461, 10.5194/acp-14-1441-2014, 2014.

Liu, M., Lin, J., Wang, Y., Sun, Y., Zheng, B., Shao, J., Chen, L., Zheng, Y., Chen, J., Fu, T. M., Yan, Y., Zhang, Q., and Wu, Z.: Spatiotemporal variability of NO2 and PM2.5 over Eastern China: observational and model analyses with a novel statistical method, Atmos. Chem. Phys., 18, 12933-12952, 10.5194/acp-18-12933-2018, 2018a.

Liu, M., Lin, J., Kong, H., Boersma, K. F., Eskes, H., Kanaya, Y., He, Q., Tian, X., Qin, K., Xie, P., Spurr, R., Ni, R., Yan, Y., Weng, H., and Wang, J.: A new TROPOMI product for tropospheric NO2 columns over East Asia with explicit aerosol corrections, Atmos. Meas. Tech., 13, 4247-4259,

10.5194/amt-13-4247-2020, 2020.

Liu, M., Lin, J., Boersma, K. F., Pinardi, G., Wang, Y., Chimot, J., Wagner, T., Xie, P., Eskes, H., Van Roozendael, M., Hendrick, F., Wang, P., Wang, T., Yan, Y., Chen, L., and Ni, R.: Improved aerosol correction for OMI tropospheric NO2 retrieval over East Asia: constraint from CALIOP aerosol vertical profile, Atmospheric Measurement Techniques, 12, 1-21, 10.5194/amt-12-1-2019, 2019.

Liu, Y.-H., Ma, J.-L., Li, L., Lin, X.-F., Xu, W.-J., and Ding, H.: A high temporal-spatial vehicle emission inventory based on detailed hourly traffic data in a medium-sized city of China, Environmental Pollution, 236, 324-333, https://doi.org/10.1016/j.envpol.2018.01.068, 2018b.

Lorente, A., Boersma, K. F., Stammes, P., Tilstra, L. G., and Muller, J. P.: The importance of surface reflectance anisotropy for cloud and NO2 retrievals from GOME-2 and OMI, 2018.

Lorente, A., Boersma, K. F., Yu, H., Dorner, S., Hilboll, A., Richter, A., Liu, M., Lamsal, L. N., Barkley, M. P., and De Smedt, I.: Structural uncertainty in air mass factor calculation for NO2 and HCHO satellite retrievals, Atmospheric Measurement Techniques, 10, 759-782, 2016.

Lucht, W., Schaaf, C. B., and Strahler, A. H.: An algorithm for the retrieval of albedo from space using semiempirical BRDF models, IEEE Transactions on Geoscience & Remote Sensing, 38, 977-998, 2000.

Naiudomthum, S., Winijkul, E., and Sirisubtawee, S.: Near Real-Time Spatial and Temporal Distribution of Traffic Emissions in Bangkok Using Google Maps Application Program Interface, Atmosphere, 13, 1803, 10.3390/atmos13111803, 2022.

Palmer, P. I., Jacob, D. J., Chance, K., Martin, R. V., Spurr, R. J. D., Kurosu, T. P., Bey, I., Yantosca, R., Fiore, A., and Li, Q.: Air mass factor formulation for spectroscopic measurements from satellites: Application to formaldehyde retrievals from the Global Ozone Monitoring Experiment, Journal of Geophysical Research: Atmospheres, 106, 14539-14550, 10.1029/2000jd900772, 2001.

Richter, A., Burrows, J. P., Nüß, H., Granier, C., and Niemeier, U.: Increase in tropospheric nitrogen dioxide over China observed from space, Nature, 437, 129-132, 10.1038/nature04092, 2005.

Shindell, D. T., Faluvegi, G., Koch, D. M., Schmidt, G. A., Unger, N., and Bauer, S. E.: Improved Attribution of Climate Forcing to Emissions, Science, 326, 716-718, 10.1126/science.1174760, 2009.

Valks, P.: Algorithm Theoretical Basis Document for GOME-2 Total Column Products of Ozone, NO2, BrO, SO2, H2O, HCHO, OClO and Cloud Properties (GDP 4.8/4.9), 2019.

Valks, P., Chan, L., Zimmer, W., Hedelt, P., and Slijkhuis, S.: PRODUCT USER MANUAL GOME-2 Total Column Products of Ozone, NO2, BrO, HCHO, SO2, H2O, OClO and Cloud Properties GDP 4.8 for GOME-2 on MetOp-A and -B GDP 4.9 for GOME-2 on MetOp-C, 2019.

van der A, R. J., Mijling, B., Ding, J., Koukouli, M. E., Liu, F., Li, Q., Mao, H., and Theys, N.: Cleaning up the air: effectiveness of air quality policy for SO2 and NOx emissions in China, Atmos. Chem. Phys., 17, 1775-1789, 10.5194/acp-17-1775-2017, 2017.

Van Geffen, J., Eskes, H., Boersma, K. F., and Veefkind, P.: TROPOMI ATBD of the total and tropospheric NO2 data products, 2022a.

Van Geffen, J., Eskes, H., Compernolle, S., Pinardi, G., Verhoelst, T., Lambert, J.-C., Sneep, M., Ter Linden, M., Ludewig, A., Boersma, K. F., and Veefkind, J. P.: Sentinel-5P TROPOMI NO₂ retrieval: impact of version v2.2 improvements and comparisons with OMI and ground-based data, Atmospheric Measurement Techniques, 15, 2037-2060, 10.5194/amt-15-2037-2022, 2022b.

van Geffen, J. H. G. M., Boersma, K. F., Van Roozendael, M., Hendrick, F., Mahieu, E., De Smedt, I., Sneep, M., and Veefkind, J. P.: Improved spectral fitting of nitrogen dioxide from OMI in the 405–465 nm window, Atmos. Meas. Tech., 8, 1685-1699, 10.5194/amt-8-1685-2015, 2015.

Vasilkov, A., Krotkov, N., Yang, E. S., Lamsal, L., Joiner, J., Castellanos, P., Fasnacht, Z., and Spurr, R.: Explicit and consistent aerosol correction for visible wavelength satellite cloud and nitrogen dioxide retrievals based on optical properties from a global aerosol analysis, Atmos. Meas. Tech., 14, 2857-2871, 10.5194/amt-14-2857-2021, 2021.

Vasilkov, A. P., Qin, W., Krotkov, N. A., Lamsal, L. N., Spurr, R., Haffner, D. P., Joiner, J., Yang, E., and Marchenko, S.: Accounting for the Effects of Surface BRDF on Satellite Cloud and Trace-Gas Retrievals: A New Approach Based on Geometry-Dependent Lambertian-Equivalent Reflectivity Applied to OMI Algorithms, Atmospheric Measurement Techniques, 10, 333-349, 2016.

Veefkind, J. P., Aben, I., McMullan, K., Förster, H., de Vries, J., Otter, G., Claas, J., Eskes, H. J., de Haan, J. F., Kleipool, Q., van Weele, M., Hasekamp, O., Hoogeveen, R., Landgraf, J., Snel, R., Tol, P., Ingmann, P., Voors, R., Kruizinga, B., Vink, R., Visser, H., and Levelt, P. F.: TROPOMI on the ESA Sentinel-5 Precursor: A GMES mission for global observations of the atmospheric composition for climate, air quality and ozone layer applications, Remote Sensing of Environment, 120, 70-83,

https://doi.org/10.1016/j.rse.2011.09.027, 2012.

Wei, J., Liu, S., Li, Z., Liu, C., Qin, K., Liu, X., Pinker, R. T., Dickerson, R. R., Lin, J., Boersma, K. F., Sun, L., Li, R., Xue, W., Cui, Y., Zhang, C., and Wang, J.: Ground-Level NO₂ Surveillance from Space Across China for High Resolution Using Interpretable Spatiotemporally Weighted Artificial Intelligence, Environmental Science & Technology, 56, 9988-9998, 10.1021/acs.est.2c03834, 2022.

Weng, H., Lin, J., Martin, R., Millet, D. B., Jaeglé, L., Ridley, D., Keller, C., Li, C., Du, M., and Meng, J.: Global high-resolution emissions of soil NOx, sea salt aerosols, and biogenic volatile organic compounds, Scientific Data, 7, 148, 10.1038/s41597-020-0488-5, 2020.

Yang, L. H., Jacob, D. J., Colombi, N. K., Zhai, S., Bates, K. H., Shah, V., Beaudry, E., Yantosca, R. M., Lin, H., Brewer, J. F., Chong, H., Travis, K. R., Crawford, J. H., Lamsal, L. N., Koo, J. H., and Kim, J.: Tropospheric NO2 vertical profiles over South Korea and their relation to oxidant chemistry: implications for geostationary satellite retrievals and the observation of NO2 diurnal variation from space, Atmos. Chem. Phys., 23, 2465-2481, 10.5194/acp-23-2465-2023, 2023.

Zhang, Y., Lin, J., Liu, M., Kong, H., Chen, L., Weng, H., and Li, C.: High-resolution Tropospheric NO2 Retrieval over Asia based on OMI POMINO v2.1 and Quantitative comparison with other products, National Remote Sensing Bulletin, 10.11834/jrs.20221413, 2022.

Zhou, Y., Brunner, D., Spurr, R. J. D., Boersma, K. F., Sneep, M., Popp, C., and Buchmann, B.: Accounting for surface reflectance anisotropy in satellite retrievals of tropospheric NO2, Atmospheric Measurement Techniques, 3, 1185-1203, 2010.